Investigation of the compound layer and diffusion zone of pulsed plasma nitrided 51CrV4-steel

Helle Berg Bjørsom

Master project
Materials, energy and nanotechnology
Department of Physics

UNIVERSITY OF OSLO

30.09.2013

Abstract

51CrV4-steel was pulsed plasma nitrided (PPN) with four sets of parameters. The resulting compound layers and diffusion zones were investigated using visible light microscopy, scanning electron microscopy, hardness measurements and x-ray diffraction.

The results showed that the four different PPN treatments resulted in four compound layers and diffusion zones with different thickness. The compound layers ranged from 0.2 µm to 2.3 µm, while the diffusion zones ranged from 62 µm to 138 µm.

The PPN treatment that was supposed to result in a sample with no compound layer exhibited a very thin surface layer of about 0.2 µm. To achieve the goal of a PPN process that result in no compound layer, the parameters have to be adjusted with either dilution of the plasma, or reduction of the nitriding time.

XRD analysis revealed that all the samples consisted of the three phases α-iron, Fe_3N and Fe_4N, and the intensities indicated different ratios.

One sample, which was PPN with a low temperature process, was investigated with transmission electron microscopy (TEM).

TEM imaging revealed grains in the size order of a few 100 nm at the compound layer surface. Electron diffraction showed extra diffraction spots corresponding to a primitive cubic lattice with a cell parameter of 6.58 Å. Further investigation is needed to decide what causes the external ordering and to create a model of the expanded unit cell.

Preface

This thesis is written as a part of the degree Master of Science in Materials, Energy and Nanotechnology. The project is a collaboration between Aker Solutions, MOTecH Plasma and the structure physics research group at the Department of Physics at the University of Oslo.

I would like to thank my supervisors Anette. E. Gunnæs (Department of Physics), Per Giltvedt (Aker Solutions) and Rune Hoel (MOTecH Plasma) for guidance and support and valuable input. Ole Bjørn Karlsen and Stefano Rubino alos deserve a mention. Without your training, insight and technical support I would never have finished.

I would also like to thank Eva Skarbøvik and Anne Jorunn Berg for valuable input and motivation.

Thanks to Aida Kazagic for being an exceptional office-room mate and for letting me vent my frustrations.

Without the support and friendship of my girls Ingrid Håøy Nygård, Ingrid Vee, Ingunn Sandberg and Torunn Kjeldstad I would not have finished my bachelor's degree, let alone this master thesis. An extra thanks to Torunn for helping me make sense of my TEM-results and to Sigrid Sognli Høyem for keeping my spirits up and cheering me on.

A special thanks go out to my family, my parents Gry Berg and Ole Peder Bjørsom and Tiril Berg Bjørsom and Eirik Berg Bjørsom. You keep me inspired and motivated!

And last, but not least, I have to thank my fiancé Njáll Ekstrøm for always believing in me and keeping me sane.

University of Oslo, September 2013

Helle Berg Bjørsom

List of Abbreviations

BSE	Backscattered electrons
DC	Direct current
EDS	Energy dispersive spectrometer
EELS	Electron energy loss spectrometer
ETD	Everhart-Thornley detector
HE	Hydrogen embrittlement
HELP-mechanism	Hydrogen enhanced local plasticity mechanism
LFD	Low field detector
Nital	HNO3 in alcohol
PIPS	Precision ion polishing system
PPN	Pulsed Plasma Nitriding
SAD	Selected area diffraction
SEM	Scanning electron microscope/y
SSD	Solid state detector
TEM	Transmission electron microscope/y
VLM	Visible light microscope
XRD	X-ray diffraction

Table of Contents

1 Introduction

1.1 Background and motivation

Steel and low alloy steel is one of the most common construction materials in use today. It is important in the manufacturing of everything from buildings, to cars, to computers and energy instalments. The petroleum industry is no exception to this. A lot of the world petroleum resources are located subsea, and low alloyed steel is the main construction material for subsea equipment.

Failures in the subsea equipment can lead to catastrophic incidents, like the 2010 Deepwater Horizon oil spill. The spill area in the Gulf of Mexico hosted 8332 different species, and the threat to the biodiversity of the region was immense [1]. Among others the spill caused major devastations to the Gulf area coral reefs. In addition to the environmental impact, failures in the equipment can cause severe risk to human life and health; and significant economic losses [2].

To achieve a comfortable living standard for everyone, the world is dependent on energy. Right now petroleum-based energy is a very important source. It is vital that the retrieval of petroleum resources is done in a safe and effective manner, to prevent damage to the environment and ensure workers' safety.

Over the recent years the development in the petroleum industry has yielded a demand for materials that can withstand crude conditions. This has led to an increased use of high strength steel alloys [3]. However, several failures have demonstrated how these alloys may be susceptible to hydrogen embrittlement (HE), and hydrogen induced stress cracking, where stress and hydrogen occlusion leads to brittle fractures at stress well below the materials yield strength. The question is; how does this happen and how can it be prevented?

The mechanisms behind HE are not completely understood, but several methods has been developed to assists engineers in handling the problem. Great care is taken during manufacturing of steel to keep hydrogen out of the materials, and strict guidelines limits the load on equipment to keep them from failure. There is still a need to find a solution that

allows the materials to be utilized at the full capacity. A reliable method to prevent HE will remove the problem entirely and thereby greatly reducing the risk of failure.

One proposed solution is to develop a barrier to prevent hydrogen from entering the susceptible material. Nitriding of the steel surface might be a method to block hydrogen and some background and earlier work on this topic is presented in 1.7.

1.2 Scope and methods

The goal of this master project is to get increased knowledge of the result of the nitriding process by investigating the compound layer and diffusion zone . The nitriding process, which is described in chapter 1.6, creates an iron nitride compound layer on the surface (typically 2-20 µm thick), whit a diffusion zone with nitrogen in solid solution with iron below it, illustrated in Figure 1-1. The diffusion zone can be up to 700µm thick and below the diffusion zone the base material is unchanged.

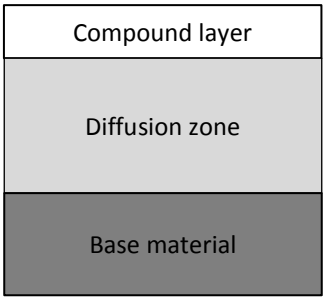

Figure 1-1: Result of the nitriding process. The compound layer in this project is less than 3 µm thick, and the diffusion zone is between 50µm and 150µm thick. Modified from [4].

Three different sets of nitriding conditions were selected, and the result of the three treatments should be three different compound layer thickness and three different sets of diffusion zone thickness. The samples and the nitriding conditions are more thoroughly explained in chapter 3.1, but a quick description is given below.

The first sample was nitrided with a process that creates a fairly thin nitride compound layer, and at the end of the process oxygen is mixed into the plasma to create a protective oxide layer on the outside. Another sample was polished smooth and nitride with the same process, but without the oxidizing step at the end.

The second nitriding condition was a new low temperature procedure. To get the required properties in steel, the material goes through a set of heating and cooling procedures until the desired properties are achieved. Any post-manufacturing treatment can alter the steels properties, and a low temperature nitriding method can therefore be utilized for materials very sensitive to post manufacturing heat treatments.

The last nitriding condition was chosen with the goal of creating a diffusion zone with no compound layer. This was done because previous work, described in 1.7, has suggested that the diffusion zone is the largest contributor to the hydrogen barrier effect in nitrided steels. The absence of a hard compound layer could also be beneficial for certain applications. This process was also a low temperature treatment.

These four samples will be imaged with light microscopy and scanning electron microscopy (SEM) to determine the compound layer thickness and uniformity. The diffusion zone will be measured using Vickers hardness indentations, and heat treatment to get the nitride in solid solution to precipitate into nitride needles will be performed.

There will also be developed a procedure for making transmission electron microscopy (TEM) samples and some preliminary electron diffraction and imaging will be conducted. Structural information about the samples will be examined using x-ray diffraction.

This master thesis will start with a theoretical introduction to hydrogen embrittlement, with a summary and discussion of the two main proposed mechanisms in chapters 1.3 to 1.5. Then the nitriding process will be described in chapter 1.6 with a description of earlier work on nitriding as a hydrogen barrier presented in chapter 1.7.

Chapter 2 contains the theory necessary to understand this project work and chapter 3 will describe the experimental methods and the procedures used for sample preparation. The results of the project are presented in chapter 4 while the findings are discussed in chapter 5.

1.3 Hydrogen embrittlement

Hydrogen embrittlement (HE) is defined as the hydrogen caused reduction of the load-bearing or the mechanical energy absorption ability of a metallic alloy [5]. The phenomenon was originally found in iron and steels and was first published in 1875 by William H. Johnson in

an article titled: “On some remarkable change in iron and steel by the action of hydrogen and acids” [6]. He writes:

“For a long time it has been well known […for…] manufacturers, who free the iron or steel […] from rust by cleaning it with sulphuric acid, that after this process the metal becomes much more brittle than before. Further, if a piece of iron wire that has been cleaned in sulphuric acid be bent rapidly to and fro till it is broken, and the fracture then moistened with the tongue, bubbles of gas arise from it, causing it to froth.”

Johnson was also a man of foresight. In the article he published in Nature in the same year he writes: *“(…) in fact, it seems probable that every property of iron or steel undergoes a change after the occlusion of hydrogen, and the extent of this change becomes a matter of great interest to the engineer now that iron and steel are so largely used.”* [7]. Now, over a hundred years later, steel is still the material of choice for most constructions and the effect of hydrogen on iron and steel is still a subject that receives great interest.

One of the identifying characteristics of hydrogen embrittlement of steels is that the material will fracture at a lower total stress in the presence of hydrogen than it would in the absence of hydrogen[8]. This will limit the loads on the material and can pose as a challenge for engineers.

1.3.1 Stress and strain

When a piece of material is subjected to a load there is force working on the piece. Stress is defined as the average force per area of material. When a material is subjected to stress it will begin to deform. Deformation along the axis of the applied force is called strain and is measured in the change in the length divided by the original length [9]. To quantify these properties a test is performed on a sample and the stress, σ, is plotted against the strain, ε, to produce a stress-strain curve, seen in Figure 1-2.

If the material is somewhat ductile and the stress is low the deformation will be elastic and the material will revert back to normal when the stress is removed. When the applied stress is higher the deformation will become permanent, and this is called plastic deformation. If even more stress is applied the material will eventually fracture [9].

In the elastic region of the stress-strain curve the relationship between stress and strain is linear, and the slope is called the elastic modulus of the material. After the elastic region the plastic region follows and the curve stops where fracture happens. The point where plastic deformation begins denotes the yield point, and this is an important value for engineers when designing equipment. Some materials do not have a yield point, so then an offset value is used instead. Typically this offset value denotes 0.2% permanent deformation. Engineers use a different type of stress-strain curve where apparent stress is plotted against strain. Apparent stress uses the original cross section of the test piece as a reference throughout the measurement. When deformation occur the actual cross section of the test piece decreases and since stress is force per area the true stress keeps increasing, even though the apparent stress decreases. Figure 1-2 is an illustration of a typical stress-strain curve, illustrating the difference between a real plot and the engineering plot. The elastic modulus and offset yield point is marked.

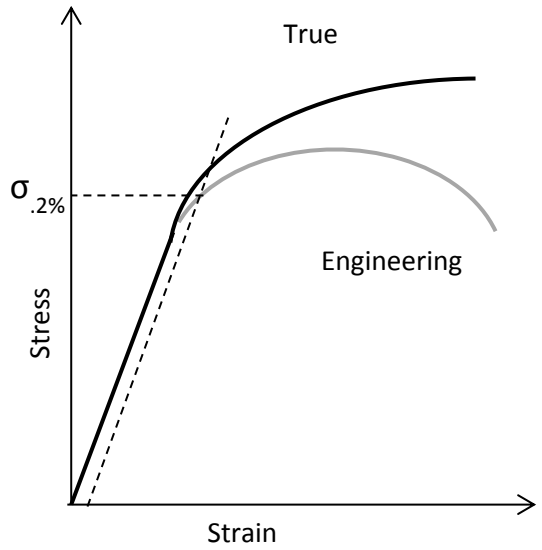

Figure 1-2: Illustration of a typical stress-strain curve for a metal. The engineering curve is apparent stress against strain, while the true curve is actual stress. The offset yield point is marked with $\sigma_{.2\%,}$ The slope of the straight line is Young's modulus, E. Modified from [10]

When hydrogen is introduced to the system these curves can look very different. Fracture can happen at a much lower stress and the regions of plasticity and elasticity can be very changed.

1.3.2 Ductile and brittle fracture

Hydrogen embrittlement is also often accompanied by a change in the fracture mode from ductile to brittle fracture, which means that fracture takes place in the elastic region, with no prior deformation at all.

Figure 1-3 gives an illustration of this. The ductile fracture shows evidence of necking and deformation, while the brittle fracture does not [11].

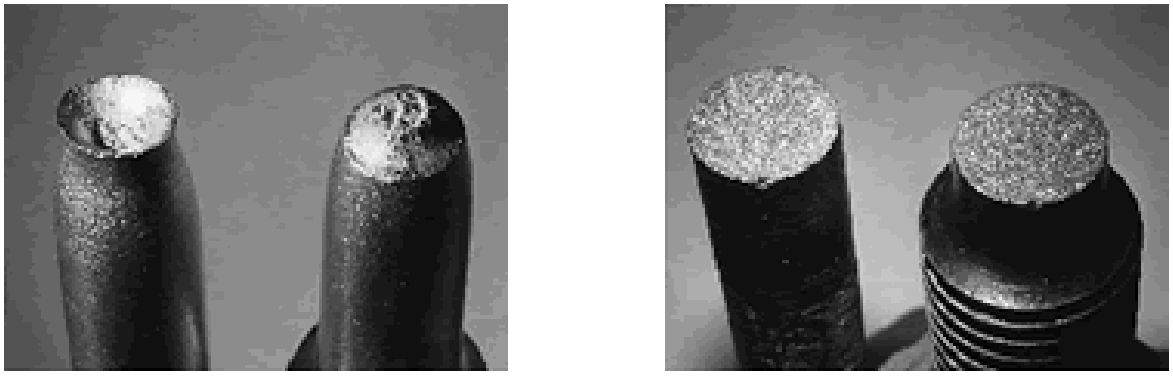

Figure 1-3: The fracture surface of a ductile fracture surface to the left and a brittle fracture surface to the right [11].

When a material gets brittle it is difficult to see damage before fracture occurs, and therefore there will be no time to repair the equipment. This can be very serious because failure can happen suddenly and the results can be catastrophic.

1.3.3 Plastic deformation and dislocations

To understand the embrittlement process that hydrogen has on a metal it is also important to understand plasticity itself and the microscopic mechanisms behind.

When a ductile material is subjected to stress there is a relative low probability of the material breaking in two due to atom planes being separated. The force needed to separate the planes in this manner is often quite high. Planes not perpendicular to the stress, however, will be subject to a shear stress that will attempt to make the planes glide relative to each other, see Figure 1-4 [9].

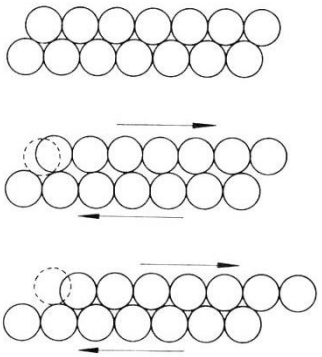

Figure 1-4: Planes gliding relative to each other [12].

The planes in the structure that starts gliding easiest are called slip planes. There are several slip systems in most structures and knowing these will give an idea of which directions (x, y, z) the materials are strongest. Figure 1-5 is an illustration of the slip mechanism of plastic deformation.

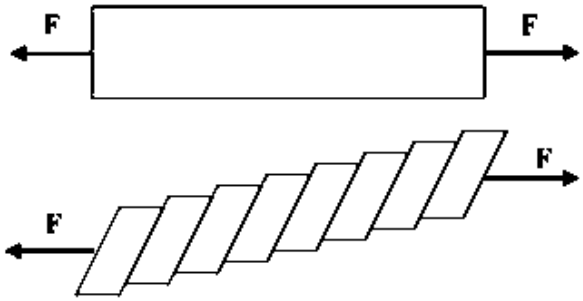

Figure 1-5: The slip mechanism of plastic deformation [13].

The cause of slip is often the movement of dislocations in the structure of the material[9]. A dislocation is a crystallographic lattice defect, and some types can be visualized as a plane of atoms terminating in the middle of a structure, see Figure 1-6. They are not thermodynamically stable and are generated by stress, precipitation, phase transformations, mechanical work or fast cooling.

The formation of dislocations often leads to the formation of more dislocations in the same or nearby planes. This leaves a large part of the structure intact and it is therefore possible to see dislocations in the microscope.

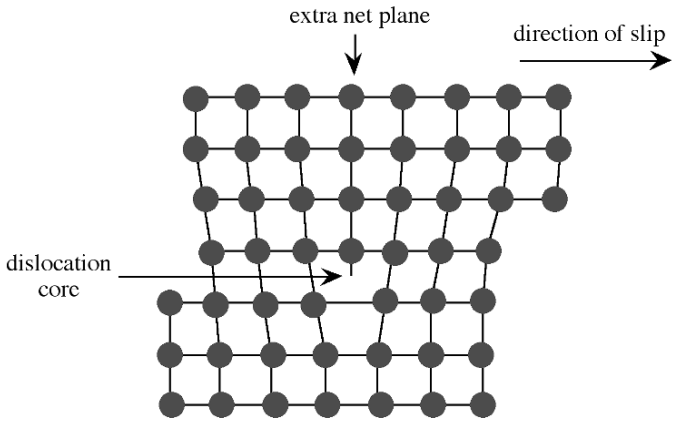

Figure 1-6: An edge dislocation defect in a lattice. Dislocations decide the direction of slip and are responsible for plastic deformation [9].

When a material is hardened the goal is to decrease dislocation movement. This can be done by introducing many dislocations so they get stuck in each other. Impurities, secondary phases or grain boundaries also trap dislocations, and will therefore make a material harder.

Since hydrogen embrittlement is an effect of material hardening these processes are important in understanding the mechanisms behind hydrogen embrittlement and will eventually be a basis for developing ways to prevent it.

1.4 Mechanisms of hydrogen embrittlement

There are several suggested mechanisms for hydrogen embrittlement [8, 14-16]. However, one single mechanism can most likely not explain all cases of hydrogen embrittlement, and the general opinion is that more than one of the mechanisms contributes in each case [17].

One proposed mechanism is the internal pressure mechanism, where hydrogen in voids in the structure induces sufficient pressure and stress to nucleate and propagate a crack. Another mechanism is the adsorption of hydrogen at crack tips which leads to lowering of surface energy. Hydrogen can also accumulate at precipitates and in second phases, which can result in dislocation formation or crack nucleation and propagation. Hydrogen may also stabilize and increase strain induced vacancies, which can lead to the formation of micro voids [14].

In situations where establishment of a high internal hydrogen pressure is improbable there are only two mechanisms considered viable [14, 16]; hydrogen enhanced local plasticity and hydrogen induced decohesion; these two options will be outlined below.

1.4.1 Hydrogen enhanced local plasticity

When the metals involved do not form stable hydrides other mechanisms are needed to explain hydrogen embrittlement. One of these mechanisms is the hydrogen enhanced local plasticity (HELP) mechanism. This mechanism is based on the observation that hydrogen enhances the mobility of dislocations [14, 15, 18].

The idea of a ductile process being responsible for a brittle fracture can seem a bit counter intuitive, but local ductile effects can indeed lead to a brittle fracture and there has been evidence of ductile processes on the surfaces of hydrogen embrittled fractures. The general opinion was, however, that this was not a result of the hydrogen itself, but rather a consequence of the effects of hydrogen on other properties.

Beachem [19] was the first to propose that the effect of hydrogen was to unlock rather than lock dislocations, he wrote: “it [hydrogen] allows them [dislocations] to multiply or move at reduced stresses”. Later Lynch[20] found evidence of dislocation activity at fracture surfaces of materials exposed to hydrogen and he proposed that the crack growth occurred by localized plastic flow.

Today the HELP mechanism is accepted as a valid mechanism of hydrogen embrittlement in some cases. Extensive studies on different materials in-situ shows dislocation movement, as the pictures in Figure 1-6 are a good example of. The figure shows transmission electron microscope pictures taken in situ from a videotape of a gathering of dislocations under varying hydrogen pressure. The separation distances between the dislocations are decreasing with increasing hydrogen pressure.

Numerous materials have been deformed in-situ in an environmental cell in a transmission electron microscope (TEM). A surprising feature of these studies is that the effect of hydrogen on the mobility of dislocations is independent of the crystal structure and is the same for edge, screw, mixed and partial dislocations [15].

Exactly how the hydrogen enhances dislocation mobility is still unknown, but one promising model is that the hydrogen induces an elastic shielding effect which enhances dislocation mobility [15]. The hydrogen forms an atmosphere around dislocations and other elastic stress centres and the atmosphere will be redistributed as the stress-fields merge. This effectively shields the dislocations from the elastic centres and reduces the interaction energy between

the dislocation and the obstacles. This allows the dislocations to move at lower levels of applied stress.

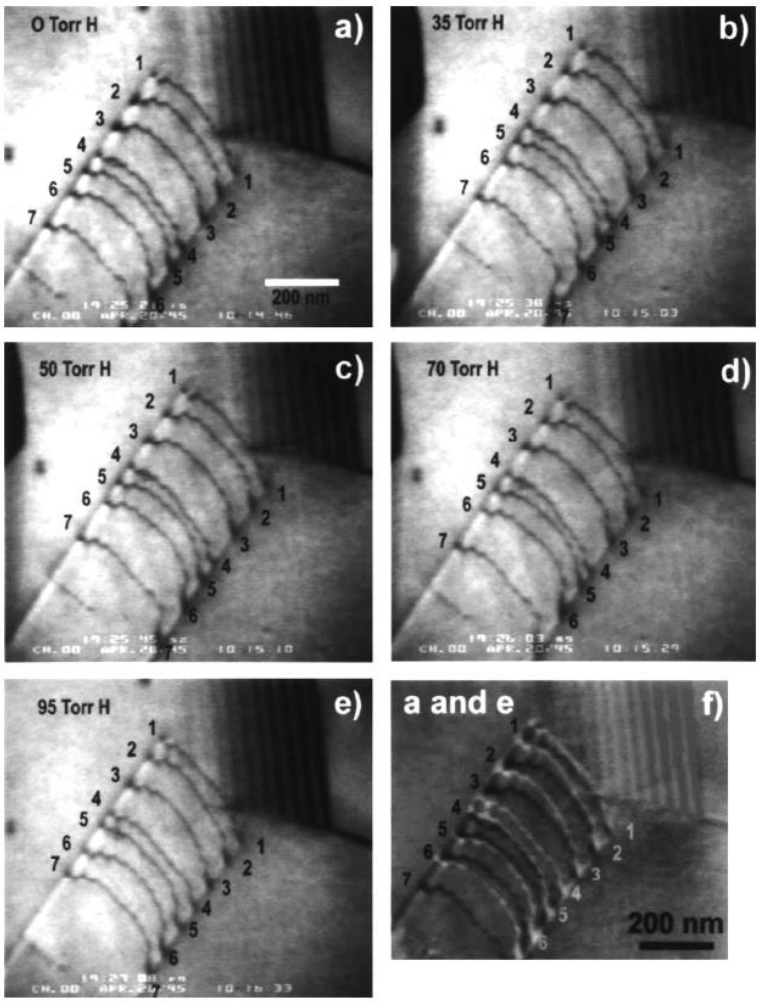

Figure 1-7: Transmission electron microscope images showing the reduction of the separation distance between dislocations in a pile-up due to solute hydrogen [18]. The material investigated is 310s stainless steel. Picture f is a superimposition of picture a and a negative image of picture e.

The HELP mechanism is debated because of some weaknesses in the supporting evidence. Most of the studies are done by TEM, which requires thin foils of materials, with thickness less than 200 nm [15, 17, 18]. At best this will give a two-dimensional stress state and there is a possibility that surface effects can influence the dislocation movement. There is also a lack of extensive studies for materials with complex microstructures with multiple obstacles and short slip distances, which are typical for high strength alloys.

1.4.2 Hydrogen induced decohesion

Another possible mechanism for metals that do not produce stable hydrides is the hydrogen induced decohesion model. In this model the mechanism of hydrogen embrittlement is assumed to be that the hydrogen within the lattice reduces the cohesive bonding strength of the solid [16, 17].

The model is based on the premise that stress will cause hydrogen to accumulate in higher concentrations than the stress-free solubility of hydrogen in the metal [21]. The accumulation of hydrogen is a result of the thermodynamics of stressed bodies, where the concentration of hydrogen will increase in areas of the material where the stress is high to keep the chemical potential of hydrogen constant.

This increased concentration of hydrogen will lower the atomic attraction between the metal atoms, and thereby the maximum cohesive force, F_m, between the two atoms, as illustrated in Figure 1-8. The cohesive force is the force needed to separate two identical molecules and to break a bond the local stress have to be greater than or equal to the cohesive force [8]. When hydrogen reduces the cohesive force, bond breaking will happen at lower local stresses and subsequent cracking will occur at lower stresses than in a hydrogen free environment. This happens along crystallographic planes, grain boundaries and particle/matrix interfaces and leads to decreased fracture toughness of the material.

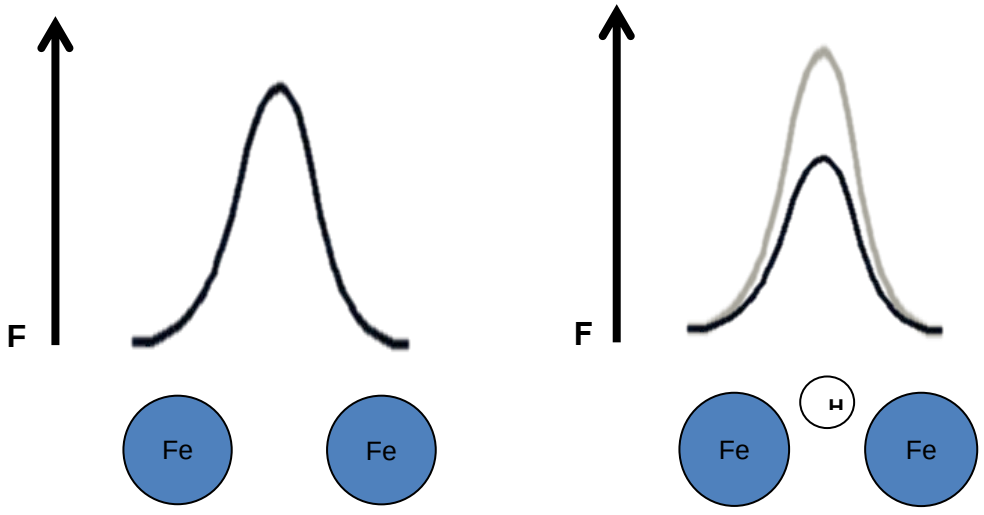

Figure 1-8: The cohesive force is the force needed to separate two identical molecules. When hydrogen accumulates in the lattice the cohesive force between two iron atoms will be lowered.

The decohesion model provides the basic notion that hydrogen damage occurs in the zone in front of the crack tip [17]. The tensile stress of the crack tip will be high and therefor there will be a lot of hydrogen accumulating in this zone. Damage sites in front of the crack tip could therefore suggest hydrogen embrittlement after the decohesion model.

Evidence for which mechanism that dominates can also be found from examining the crack tip opening-angle of cracks propagating in both a hydrogen atmosphere and in vacuum. Certain crystal structures have certain slip systems and when the angle between these systems is known it can be used to evaluate if the crack propagates by slip mechanisms or another mechanism.

Vehoff and Rothe [22] strained single crystals of FeSi in both vacuum and hydrogen and investigated the crack tip openings, see Figure 1-9. In vacuum, the crack tip opening angle was 70°, which corresponds to the angle between slip systems, suggesting crack propagation by slip. The angle decreased after straining in hydrogen, suggesting that another mechanism dominates crack propagation in a hydrogen atmosphere.

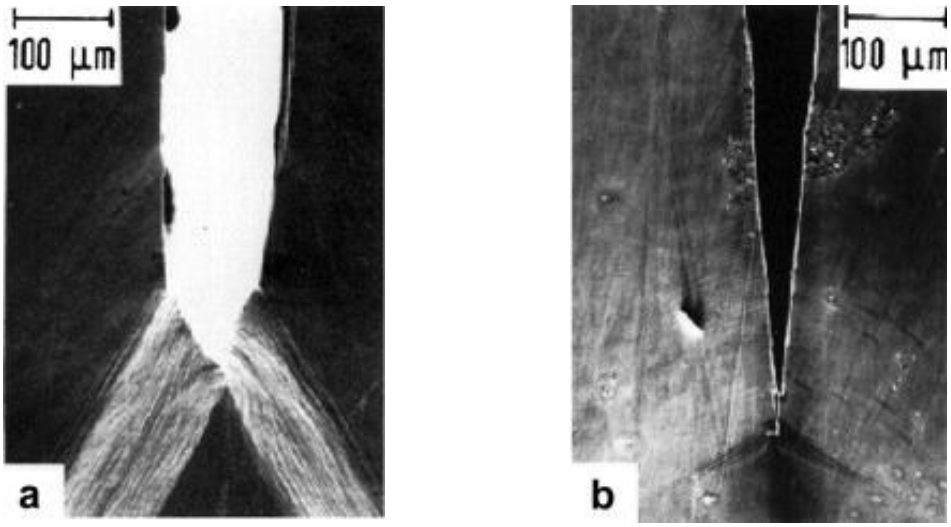

Figure 1-9: Crack tip opening angles of FeSi. Picture a) shows the angle after straining in vacuum and b) after hydrogen exposure [22]. The decrease in angle suggests a change from crack propagation by slip to another mechanism in hydrogen.

There is still a need for the decohesion model to describe the local stress in the structure with macroscopic parameters and it is also important to derive an expression for how the maximum cohesive force, F_m, varies with hydrogen concentration, chemical potential, alloy structure and interfaces structure [8].

The decohesion model is also debated because of weaknesses in the supporting evidence [8, 17]. One of the problems is that the amount of hydrogen that can be dissolved in a specimen for measurements of bulk properties is much lower than the assumed concentration of hydrogen in the fracture zone ahead of the crack tip. There is also no direct experimental demonstration that hydrogen dissolved in metals lowers the interatomic bonding strength, but DFT simulations have suggested that this could be the case [5].

1.5 Diffusion theory

In order to obtain hydrogen embrittlement the atomic hydrogen needs to come in contact with the susceptible materials surface. The entry and transport of foreign elements in a solid is called diffusion. In crystalline solids the diffusion takes place because of the presence of defects, such as vacancies and interstitial atoms [23]. Diffusion also takes place along 1- and 2- dimensional defects such as grain boundaries, surfaces and dislocations, and hence the microstructure of the solid is important.

The rate at which an element diffuses into a solid is determined by the diffusivity of the element in that solid. Under steady-state conditions the diffusivity, or the diffusion coefficient, is obtained by using Fick's first law [24]

$$J_i = -D_i \frac{dc_i}{dx} \qquad \textbf{(1-1)}$$

where J_i is the flux, D_i is the diffusion coefficient, c_i is the concentration of atoms type i, and x is the position in the solid. In iron the permeation rate, i_p^∞, of hydrogen through a uniform membrane of thickness L can be described by Fick's first law as follows[25]

$$i_p^\infty = \frac{D_{Fe} C_{0,Fe} F}{L} \qquad \textbf{(1-2)}$$

Where $C_{o,Fe}$ is the hydrogen concentration at the entry surface, D_{Fe} is the diffusivity of hydrogen in iron and F is Faraday's constant.

To prevent hydrogen embrittlement the steel can be modified to reduce the permeation rate either by reducing the concentration of hydrogen in at the surface or by lowering the diffusivity of hydrogen in iron.

1.6 Pulsed plasma nitriding

Nitriding is a surface treatment that diffuses nitrogen into the steel, creating a case hardened surface [26]. This will increase the surface hardness and improve the protection of the steel from wear and tear and in many cases corrosion properties will also improve. Nitriding can also be used as a barrier to prevent hydrogen from entering the metal and thus prevent hydrogen embrittlement [25-29].

During the nitriding process the nitrogen diffuses into the steel surface and reacts with iron, forming a compound layer consisting of iron nitrides and then a diffusion zone of nitride precipitates and/or nitrogen in solid solution with the base steel. Figure 1-1 is an illustration of the layered result of the nitriding process.

The compound layer consists of γ' iron nitride (Fe_4N) and ε-iron nitride ($Fe_{2-3}N$), the structure of these nitrides will be described in 1.8 [30, 31]. The ratio between the two nitride phases is decided by the carbon content of the steel, or the amount of nitrogen present during the nitriding process. The compound layer can be called a "nitride ceramic" and is also called the "white layer", because it stays white when the steel is etched with Nital (HNO_3 in alcohol).

The compound layer is very hard and the hardness depends on the alloying elements in the steel. The hardness increases with nitride-forming alloying elements such as aluminium, molybdenum, chromium and tungsten, but these alloying elements also decrease the case hardening depth [30]. Nitrided alloyed steels typically have surface hardness ranging from 700 HV to more than 1000 HV.

Below the compound layer there is the diffusion zone containing nitrogen in solid solution with the base steel, see Figure 1-10 for an illustration of possible nitrogen positions in the a BCC-steel lattice. In addition, the diffusion zone has stable metal nitrides formed by the various alloying elements of the steel. Because of these metal nitrides, the diffusion zone is harder than the base metal and therefore hardness measurements can be used to determine the diffusion zone depth, called the case depth.

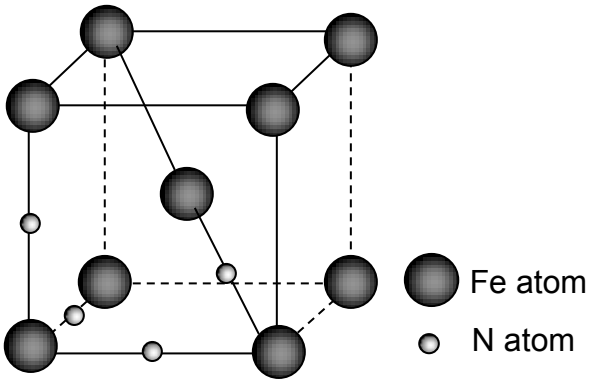

Figure 1-10: Illustration of possible Nitrogen positions in a BCC-iron lattice [4].

The pulsed plasma nitriding technique is conducted in a vacuum furnace, as depicted in Figure 1-11. The process uses the direct current (DC) glow discharge phenomenon to introduce elemental nitrogen into the surface of metallic pieces [26, 28, 32]. In the normal state gas is nonconductive. This is changed by low pressure or high voltage, which causes lightning or glow discharge to appear [33]. The gas is then changed into ionized plasma that conducts electricity.

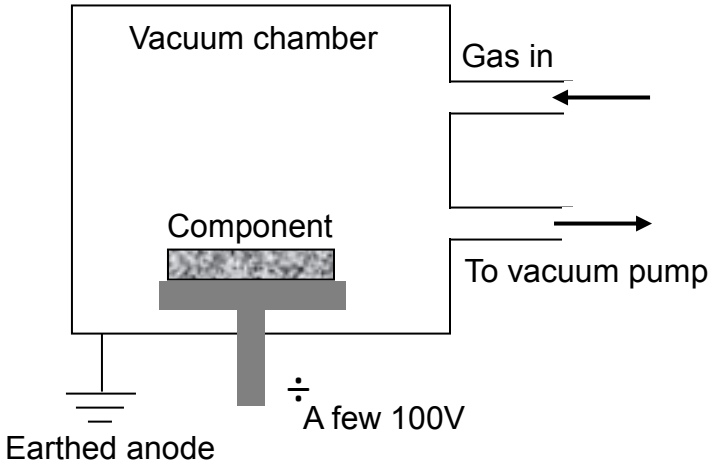

Figure 1-11: Schematic drawing of the vacuum furnace used in the pulsed plasma nitriding process [4].

The sample to be nitrated is placed in a vacuum chamber with an atmosphere of different gases at a pressure of 1-10 mbar. The metal sample will work as a cathode in relation to the vacuum chamber, which acts as an earthed anode. The high potential between the chamber walls and the sample ionizes the gas and the positive ions are accelerated and hit the sample surface with kinetic energy, Figure 1-12 is an illustration of this process. About 90% of this

energy is transformed to heath and warms the surface up to the nitriding temperature [33]. This temperature can be controlled by electric power.

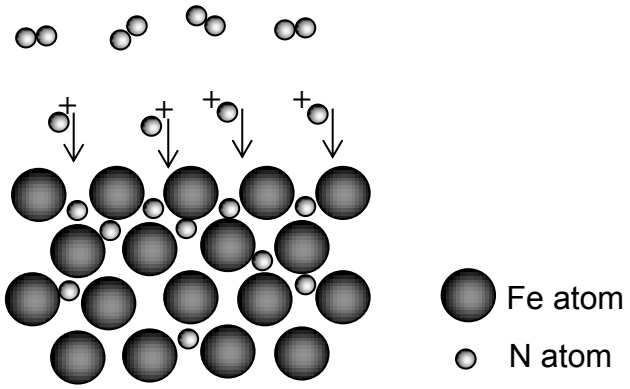

Figure 1-12: Illustration of the plasma nitriding process where the positive nitrogen ions are accelerated towards the negatively charged iron surface [4].

The nitrogen ions in the plasma are highly reactive and are attracted to the negative surface of the sample [33]. Nitrides start to form on the surface and because of the low temperature lower nitrides are produced. The nitrides create a case hardened compound layer. As FeN molecules decompose into Fe_2N, Fe_3N and Fe_4N, nitrogen is released. This nitrogen either diffuses into the sample or returns to the plasma. The nitrogen that diffuses into the sample f is in solid solution with the iron, possible nitrogen positions are illustrated in Figure 1-10.

If the sample contains nitride-forming alloying elements, nitride complexes with these elements are also formed at the surface. Chromium nitride is very hard and contributes greatly to the increased toughness and hardness of the nitrided surface [34].

By changing the temperature, plasma and length of the process the thickness of both the compound layer and diffusion zone can be controlled.

1.7 Nitriding as a method to prevent HE

While diffusion through an iron membrane can be described by equation (1-2), a nitrided membrane can be roughly treated as a three-layer membrane. This three layer membrane consists of the compound layer, diffusion layer and base steel with thickness denoted as L_c, L_d and L_{Fe} respectively [25]. The layers have different diffusion coefficients, which can be denoted as D_c, D_d and $D_{Fe.}$ The compound layer and diffusion layer are not homogenous, so the diffusion coefficients may vary with the distance from the surface. However, to get a

simplistic model the diffusion coefficients can be viewed as the as the average mobility of hydrogen in the compound and diffusion layers, respectively. The permeation rate, i_p^{∞}, of hydrogen through a nitraded membrane of thickness $L=L_c+L_d+L_{Fe}$ can be described as follows

$$i_p^{\infty} = \frac{D_{eff} C_{0,c} F}{L} \qquad \textbf{(1-3)}$$

Where $C_{0,c}$ is the concentration of hydrogen at the compound layer surface, F is Faraday's constant and D_{eff} is the effective diffusivity across the whole membrane. PPN of the steel surface affects both the entry and transport of hydrogen in the steel. This corresponds to the surface concentration and diffusivity in equation (1-3). Studies have shown reduced permeation of hydrogen through a nitrided iron membrane [25-29].

The reduction of hydrogen entering the steel is called the surface effect and is caused by the nitride compound layer [25, 28, 29]. This effect can be related to the relatively small number of sites engaged in the hydrogen entry process in the compound layer.

The reduced diffusivity of hydrogen in the compound and diffusion layer is called the barrier effect. The reduced diffusivity can be attributed to a lower solubility of hydrogen in the compound layer and to its slower transport due to trapping at nitride precipitates [25, 28]. Nitrogen is also occupying possible interstitial positions for hydrogen, and thus hydrogen mobility is reduced. Since the compound layer is relatively thin, the thicker diffusion zone has a much stronger effect on the hydrogen trapping [28].

Nitriding can also reduce HE by changing the mechanical properties of the material. Nanomechanical evaluation has showed that electrochemical H-charging of PPN austenite results in a softening of the compound layer [35-37]. In an untreated sample the hydrogen charging increased the hardness and reduced the stress required for dislocation nucleation. . The softening or hardening effect of hydrogen was dependent on nitrogen concentration and dislocation density and this effect can be used to control HE by designing an appropriate PPN process for the material in question.

1.8 Iron nitride structure

Iron exists in different allotropes and at atmospheric pressure three forms exists: α-iron, γ-iron and δ-iron [24]. These allotropes are all cubic. At high pressures a forth, hexagonal allotrope, ε-iron, exists.

At room temperature pure iron exists as α-iron, which has a body-centric cubic lattice. Different alloying elements can be dissolved in different amounts in the iron allotropes and can cause steel to adopt a γ-iron configuration.

The structures of the iron nitrides resembles the different iron allotropes, with nitrogen filling up voids in the structure, and are named after the allotrope of iron the structure resembles. The compound layer of PPN steel consists of γ' iron nitride (Fe_4N) and ε-iron nitride ($Fe_{2\text{-}3}N$) and the structures of these compound will be described below.

The structure of γ' iron nitride can be visualized as γ-iron with an extra nitrogen in the centre [38]. The correct description, however , is a primitive cubic cell, with space group number 221 - $Pm\bar{3}m$ [39]. The cell parameter a=3.97 Å and the density of the compound is 7.24 g/cm^3.The nitrogen is placed at $(0,0,0)$ and the iron atoms at $(\frac{1}{2},\frac{1}{2},\frac{1}{2})$ and $\left(\frac{1}{2},0,0\right)$, as illustrated in Figure 1-13

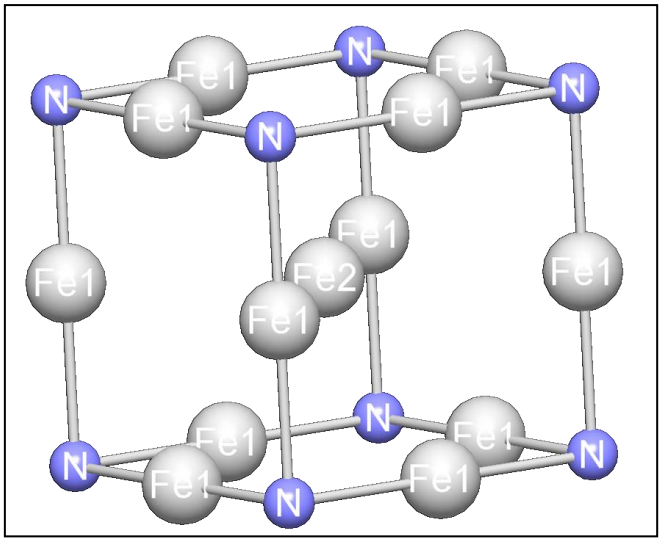

Figure 1-13: Illustration of the Fe4N unit cell. The lattice is primitive and space group is number 221 - $Pm\bar{3}m$. Nitrogen is marked with blue spheres.

The unit cell of ε-iron is hexagonal and the space group is number 182 - $P6_322$ [39], as illustrated in Figure 1-14 The lattice parameters are a = 4.71, b = 0.4.71 and c = 0.4.39. The density of the compound is 7.16 g/cm^3.

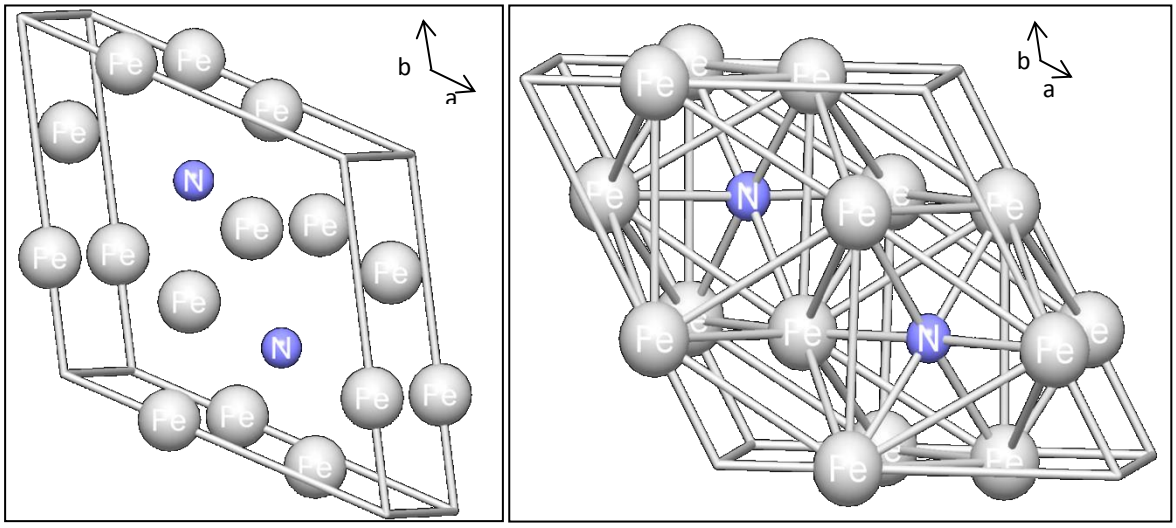

Figure 1-14: Illustration of the Fe_3N unit cell. The lattice is hexagonal and the space group is number 182 - $P6_322$ (182). Nitrogen is marked with blue spheres and in the image to the right bonds between atoms are indicated.

2 Theory

2.1 Crystallography

The way atoms or molecules in a material are organised gives important insight in the materials properties. A material can be amorphous, where there is only short range order, or crystalline, with long range ordering of the atoms.

The smallest repeating unit in a crystal is called a basis. When the basis in a crystal structure is replaced by a mathematical lattice point we get what is known as a Bravais lattice. There are a total of 14 Bravais lattices, which are presented in Figure 2-1.

The position of an atom in the unit cell can be described by a vector **r**

$$\boldsymbol{r} = x\boldsymbol{a} + y\boldsymbol{b} + z\boldsymbol{c} \qquad \textbf{(2-1)}$$

Where **a**, **b** and **c** is the lattice vectors.

2.1.1 Reciprocal space

The reciprocal lattice is a mathematical representation of the crystal in the reciprocal space. This is important for understanding and extracting information from diffraction techniques. Each point in reciprocal space represents a plane in real space. The relationship between the reciprocal lattice vectors, **a*, b*** and **c***, and the real space lattice vectors, **a**, **b** and **c**, is given by

$$\boldsymbol{a}^* = \frac{\boldsymbol{b}x\boldsymbol{c}}{V}, \boldsymbol{b}^* = \frac{\boldsymbol{a}x\boldsymbol{c}}{V}, \boldsymbol{c}^* = \frac{\boldsymbol{a}x\boldsymbol{b}}{V}, \qquad \textbf{(2-2)}$$

where V is the volume of the unit cell.

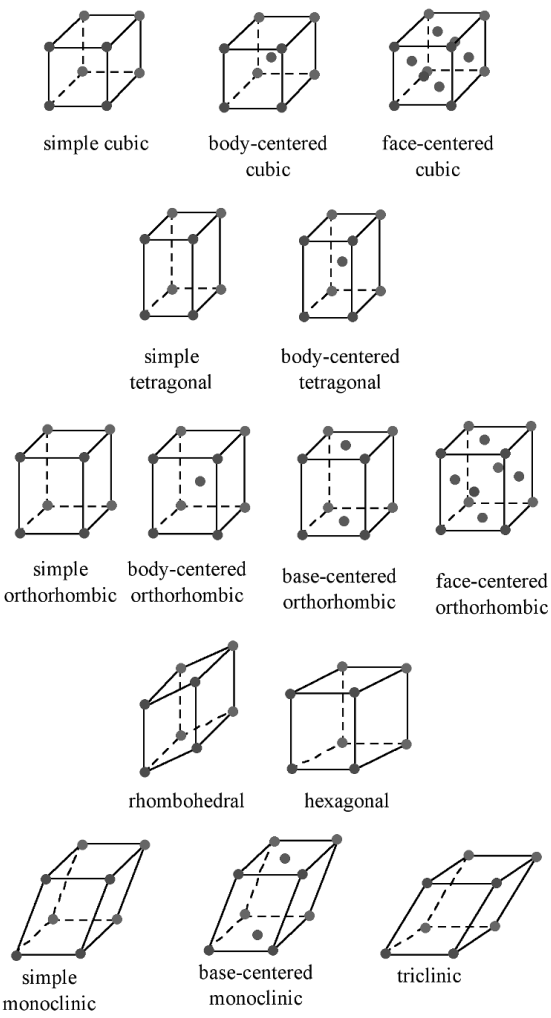

Figure 2-1: The 14 different Bravais lattices [40].

2.1.2 Lattice planes and Miller indices

A plane in a unit cell is described by Miller indices. The indices are given as (*hkl*) and indicate where the plane intersects the lattice vectors. The values are inverted so the plane (*hkl*) intersects the lattice vectors **a**, **b** and **c** at 1/*h*, 1/*k* and 1/*l*, respectively. If the plane is not intersecting a vector it has the index 0. Negative indices are written with a bar over the number, for example $(\bar{1}00)$. Planes that are equivalent are represented with {hkl}

Directions in a crystal can be represented with a vector, **r**, given by

$$\boldsymbol{r} = u\boldsymbol{a} + v\boldsymbol{b} + w\boldsymbol{c} \qquad \textbf{(2-3)}$$

Where **a**, **b** and **c** are the unit vectors. The direction is denoted as [uvw]. If [uvw] is parallel to the intersection of two lattice planes it is a zone axis.

Every plane (*hkl*) can be represented with a reciprocal vector, $\mathbf{g}_{hkl}$. This vector is normal to the plane and is defines as

$$\boldsymbol{g}_{hkl} = h\boldsymbol{a}^* + k\boldsymbol{b}^* + l\boldsymbol{c}^* \quad \textbf{(2-4)}$$

Where **a***, **b*** and **c*** are the reciprocal lattice vectors. The distance between two planes can then be given as

$$d_{hkl} = \frac{1}{|\boldsymbol{g}_{hkl}|} \quad \textbf{(2-5)}$$

For cubic crystals the distance between two planes have the following relation to the lattice constant, a:

$$d_{hkl} = \frac{a}{\sqrt{h^2+k^2+l^2}} \quad \textbf{(2-6)}$$

When indexing a diffraction pattern the notation *hkl* is used and corresponds to the point in reciprocal space representing the plane (*hkl*).

2.2 Diffraction

Diffraction is the physical phenomenon of waves scattering of a periodic lattice. At a set wavelength there will be a certain incident beam angle and lattice spacing that will give constructive interference and a diffraction pattern can be produced.

If the beam angle and the wavelength are known, the lattice spacing can be deduced from the diffraction pattern.

2.2.1 Electron and x-ray diffraction

When diffraction are used in material science to determine crystal structures the periodic lattice consists of atoms, and the waves that scatter are commonly x-rays and electrons. Atoms interact in different ways with x-rays, electrons and neutrons, so different techniques will give different information.

X-rays have an electromagnetic field that interacts that causes the electrons of an atom to oscillate with the same period as the x-rays. This oscillation will send out a field with the

same wavelength and phase as the incident x-ray beam, and this field is the scattered wave [41].

There are no lenses for x-rays so x-rays cannot be used to image the sample at the same time as giving diffraction information.

If electrons are used in diffraction they will interact much stronger with the sample. There are strong columbic forces between the negative electrons in the electron beam and the negative electrons and positive cores of the atoms. The electrons are scattered from both the core of the atoms and the electrons surrounding them.

2.2.2 Laue equations

The idea of using diffraction to probe the atomic structure of materials was credited to the German von Laue in 1913 [41]. Von Laues idea was that electromagnetic rays with a shorter wave length than visible light would cause diffraction or interference phenomena in a crystal, and he was right.

Von Laue argued that the diffracted waves are in phase if the path difference between waves scattered by adjacent scattering centres is a whole number of wavelengths. This path difference is denoted $h\lambda$, where h is an integer.

If there is two scattering centres at a distance a from each other, and an incident plane wave with wavelength λ hits the line between the two scattering centres with an angle of θ_i, the wave will be scattered. If the diffracted plane waves angle is θ_d, the path difference will be $a(\cos\theta i - \cos\theta d)$. This is illustrated in Figure 2-2.

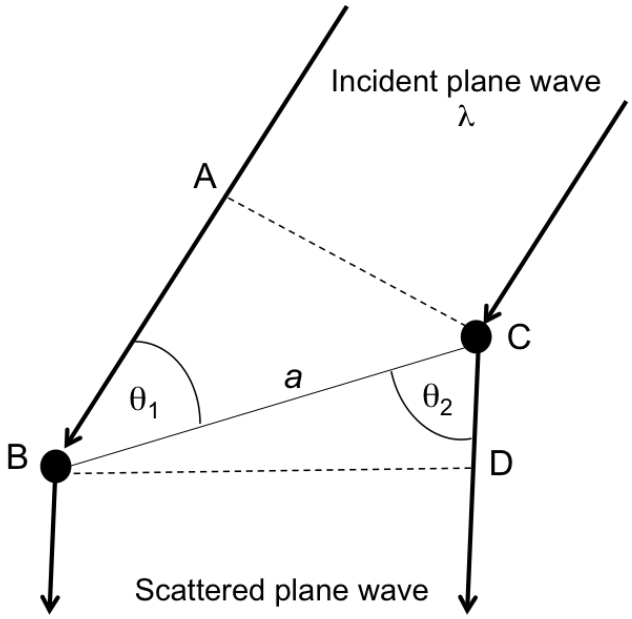

Figure 2-2: Illustration of the Laue scattering event [42].

To create constructive interference this path difference has to be equal to hλ, and the equation becomes:

$$a(cos\theta_1 - cos\theta_2 = h\lambda \quad \textbf{(2-7)}$$

In three dimensions two more Laue equations can be written, to account for two more distances, b and c, and two more sets of angles

$$b(cos\theta_3 - cos\theta_4 = k\lambda \quad \textbf{(2-8)}$$

$$c(cos\theta_5 - cos\theta_6 = l\lambda \quad \textbf{(2-9)}$$

These are known as the Laue conditions and when all three of them are satisfied simultaneously a diffracted beam will be produced from a three dimensional crystal structure.

2.2.3 Bragg diffraction

At the same time as von Laue published his conditions, father and son Bragg published a simpler view on diffraction [41]. They proposed that waves behaved as if they were reflected of atomic planes.

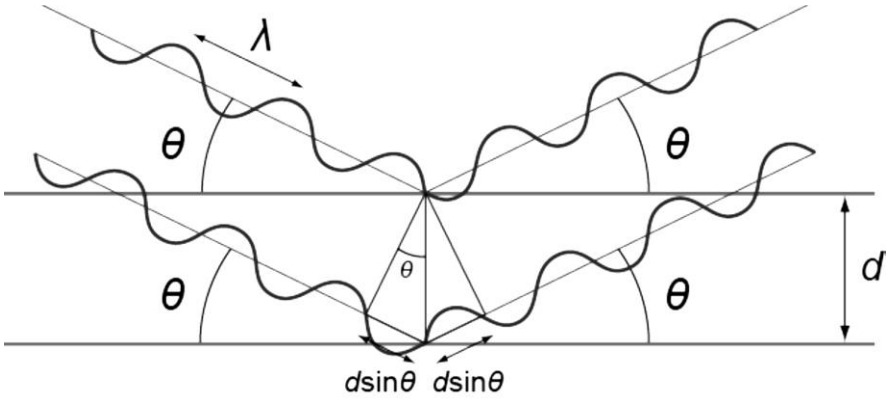

Figure 2-3: Illustration of Bragg's law[43]. To get constructive interference the waves have to be in phase after the scattering event. The difference in path length for the two waves is 2dsin(θ) and this distance must be equal to an integer number of wavelength.

When an incident plane wave hits an atomic layer the waves will be scattered. It is assumed that the layer of atoms acts as a mirror and that the refracted wave will have the same angle as the incident wave. To get constructive interference between a beam reflected of an underlying atomic layer and the beam reflected of the top layer, the two waves must be in phase. The difference in path length must then be equal to a whole number of wavelengths. This is illustrated in Figure 2-3. If the spacing between the two atomic layers is denoted d, and the incident angle and scattering angle is denoted θ, the path difference equals 2d sinθ. This leads to Bragg's equation:

$$2dsin(\theta) = n\lambda \qquad \textbf{(2-10)}$$

2.2.4 Kinematic and dynamic scattering

Kinematic scattering is when the incident electron beam is scattered only once. This can be compared to dynamic scattering when multiple scattering events can take place. With kinematic scattering the diffracted intensities reflects the crystal structure of the scattering material, but if a strongly scattered wave meet the Bragg-conditions of another set of planes this wave can be diffracted back into the direct beam and therefore give different intensities to the observed diffraction spots. This can happen for diffraction with electrons since they interact strongly with matter [41]. The probability for dynamical scattering increases with sample thickness.

2.2.5 Conditions for reflections

The kinematic scattering from an atom depends on the form factor, $f_{i,}$ the atom number Z and the scattering angle. In a crystalline compound the intensities of the diffraction spots will be determined by the structure factor F(hkl), presented in equation (2-11).

$$I = |F(\theta)|^2 = \left|\sum_i^{\infty} f_i e^{2\pi i(hx_i+ky_i+lz_i)}\right|^2 \quad \textbf{(2-11)}$$

Where x_i, y_i and z_i are the positions of atoms and hkl is a plane in the crystal. The equation summarizes the scattering from all the atoms in the unit cell. This expression can become 0 for certain hkl-values, depending on the position of the atoms. These diffraction spots will not be visible under kinematic scattering conditions.

3 Experimental methods

3.1 Description of samples

The samples used in this project are 51CrV4 steel with four different pulsed plasma nitriding (PPN) treatments. Aker Solutions provided the sample components and MOTecH Plasma did the PPN. The chemical composition of the sample steel is presented in Table 3-1.The samples are cut from two large steel components into 2 cm thick strips. Figure 3-1 is an image of this strip. Table 3-2 gives an overview of all the samples used in this project.

Table 3-1: Chemical composition of 51CrV4-steel.

Material desigantion	DIN material number	Chemical composition in percent by mass (reference values)						
C	Si	Mn	P ≤	S ≤	Cr	Mo	V	Al
50/51CrV 4	1.8159	0.51	0.28	0.90	0.035	0.035	1.05	0.15

One set of samples are cut from a sand blown component which had been PPN. The process used is a medium temperature process, taking place between 440°C and 500°C. The parameters for this PPN treatment create a thin compound layer, and at the end of the process some oxygen was mixed into the plasma to create an oxide layer for extra corrosion protection and reduced friction. This sample is called the rough surface sample, and its nitriding treatment is condition 1.

The sand blown surface proved to be too rough for TEM sample preparation. When thinning the rough surface would create big holes before electron transparency was achieved. The surface of the component was not completely flat and preparation of cross section samples where impossible because the surfaces could not be glued together. A new set of samples had to be prepared, ground flat and polished to make TEM-sample-preparation possible. Another sand blown component was cut into strips and then the surface was wet ground with SiC papers with EFPA-grain numbers from 180-2400 to make the surface flat, even and smooth.

The polished samples where then PPN with three different sets of parameters. One sample was PPN with the same parameters as the sand blown sample, but without an oxidation step at the end of the process. This sample is the smooth surface sample, nitride under condition 1.

The two last samples were nitrided with a low temperature process, taking place at a temperature below 440°C. To compensate for the lower temperature the nitriding time was increased by a factor of 3 compared to PPN condition 1. One of the two samples was PPN with the same plasma as the samples PPN with condition one and this sample is called the low temperature sample and the PPN is condition 2.

The last sample was PPN with the goal of creating a sample with no compound layer, so this sample was PPN with diluted plasma. The nitrogen was diluted by a factor of 12 compared to the other samples. The plasma was diluted by mixing in hydrogen. This sample is called the no-compound layer sample and the PPN is condition 3.

Table 3-2: Overview of the four different samples used in this master project and the differences in the nitriding parameters.

Sample	Reference number	Temperature	Time	Plasma composition	Surface roughness
1 - Rough	11915	440-500°C	t	N + O	Sand blown
1 - Smooth	32128	440-500°C	t	N	SiC #2400
2 – Low T	32129 TEXEL	<440 °C	3t	N	SiC #2400
3 – No CL	32130	<440 °C	3t	Diluted: N/12	SiC #2400

After PPN the sample pieces were cut into smaller pieces, taken from the bottom of the strip, which corresponds to the inside of the steel component, see Figure 3-1. The bottom parts where used for hardness-measurements, SEM-imaging and light microscope imaging. The middle parts were used for diffraction measurements and TEM-imaging.

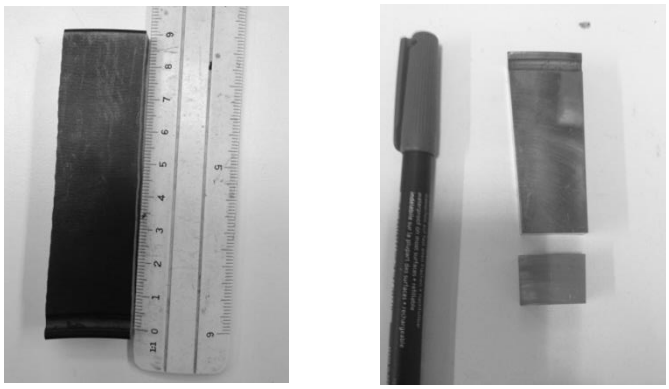

Figure 3-1: The sample material was cut into approximately 2 cm thick strips, which was then polished. The polished and nitrided samples where then cut into pieces, taken from the inside of the larger component. The picture is of the piece cut for diffraction measurements and TEM-imaging.

In an effort to image the diffusion zone, a piece from each of the polished and PPN samples where heated at 400° C for 25 minutes. This should cause the nitrogen in solid solution in the diffusion zone precipitate into γ'- iron nitride needles which might make the diffusion zone visible in the visible light microscope or the SEM [30].

3.2 Visible light microscopy

The visible light microscope (VLM) uses visible light and a collection of lenses to magnify an object. When the object is not transparent to light, a microscope type where the image is created by reflected light from the objects surface is used.

The VLM was used to determine the thickness and evenness of the compound layer, since the compound layer is of a size order that can be imaged with visible light.

To image the nitride compound an etchant named Nital is used. This etchant reveals grain boundaries in austenite (not applicable in this project) and highlights different phases. The nitride compound layer will appear white in the microscope after etching. Oxide layers will appear dark [30].

3.2.1 VLM instrument

A Reichert-Jung MeF3 microscope was used and the images where captured using a Jenoptik ProgResC5 CCD camera. The images where edited and enhanced using Adobe Photoshop or Microsoft Office. The edition consisted of changing the brightness and contrast of the images to enhance the nitride compound layer. The layer thickness was measured using the program ProgResCapture, which is also the program that the images are taken with.

3.2.2 Sample preparation for VLM

To get a good image of the sample it needs to be polished to a mirror-like finish. The surface should be scratch-free, free from smear, drag, or pull-outs and with minimal deformation remaining from the preparation process. If this surface is viewed in the light microscope the sample will look like a plane white surface. To highlight features of the metal microstructure an etchant is used. The etchant will corrode away certain parts of the sample, revealing grain boundaries, highlight different phases or inclusions in the metal.

The samples where cut into pieces of about 1 x 2 cm and were then mounted with DuroCit powder and DuroCit liquid cold mounting material. The samples were taken from the inside of the large sample piece, see Figure 3-1. The samples where mounted to give a cross section view of the nitride compound layer and diffusion zone. This makes it possible to image the compound layer, do compositional analysis across the cross section and investigate hardness differences across the diffusion zone. Since the nitride layer is very hard sample preparation can damage the compound layer. A hard mounting material was chosen to limit damage and improve edge retention.

The samples were prepared using Struers procedure for preparation of nitrited steels which is described below [30]. First the deformation from cutting of the samples was removed using a Pedemax-2 wheel grinder with SiC-paper of EFPA #220 grain number. The force applied was 150 N and the grinding speed was 300 rpm.

The samples were then grinded with a 9 µm colloidal diamond suspension and a hard surface. Then the samples where polished in two steps with colloidal diamond suspensions containing particles 3 and 1 µm and appropriate soft polishing cloths. The samples where rinsed with water and dried with pressured air between each step. The force applied was 150N and the grinding speed 150 rpm.

Before examining the samples in the VLM they were etched with 4% Nital (HNO_3 in ethanol) to expose the microstructure and nitride compound layer.

3.3 Scanning electron microscopy

Scanning electron microscopy (SEM) is a technique where an electron beam is scanned over a given area of a sample and where electrons and x-rays generated by the interaction are used to make an image or analysed to give chemical information.

There are three main types of signals that are collected and analysed when using a SEM, see Figure 3-2 for an illustration of their origin. Secondary electrons are low energy electrons created by electrons colliding with the outer shell of an atom. Back scattered electrons are scattered from the electric field surrounding the core of the atom and can therefore give some information about different phases as heavy core will scatter more electrons than a lighter core. X-rays are generated when the electron beam removes an inner shell electron and an

outer shell electron fills that hole while sending out energy in the form of a photon. These energies are characteristic for the different elements and can be used to decide the chemical composition of a sample.

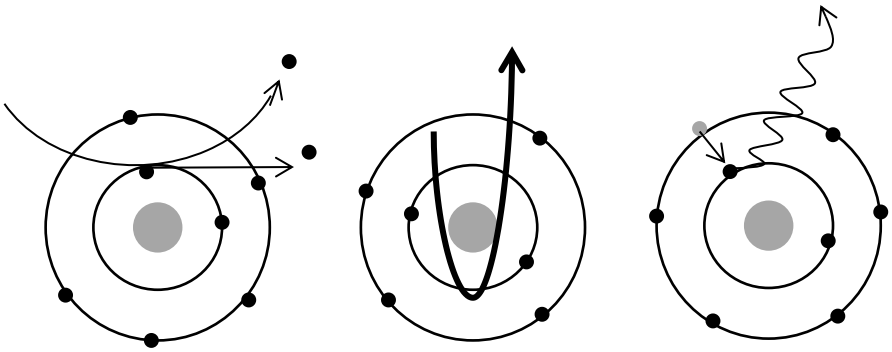

Figure 3-2: To the left the creation of a secondary electron, in the middle a backscattered electron and to the right the generation of a characteristic x-ray is illustrated. Modified from [44].

The different signals have different energies and therefore they originate from different depths of the sample, see Figure 3-3. Secondary electrons from about 10 nm into the sample can be detected; the backscattered electrons have a bit higher energy and can originate from depths up to 2 μ, while the electron-excited characteristic x-rays can come from volumes that are located up to 5 μm into the sample.

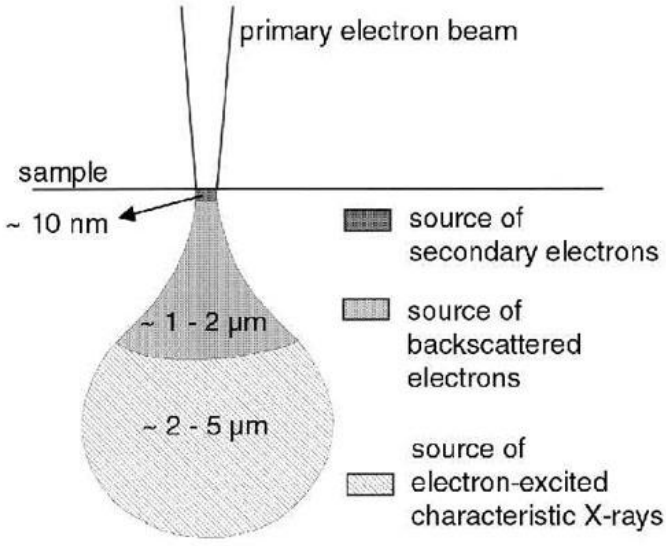

Figure 3-3: The interaction volume of the different signals used in scanning electron microscopy [45].

The energy of the beam and the samples composition determine the size of the interaction volume. A higher energy beam will enlarge the overall interaction volume and will enable information from deeper into the sample to be collected. A lower energy beam will give information from the surface, but the resolution is lower and the count frequency for x-ray collection is lower. The electron range, R, can be used to calculate the interaction volume and can be calculated using [46]:

$$R = \frac{0.0276\ A\ E_0^{1,67}}{\rho Z^{0.89}} (\mu m) \quad \textbf{(3-1)}$$

Where A is the atomic weight, Z the atomic number, ρ the density and E_0 the energy of the electron beam. For iron (A=55.85, Z=26, r=7.87) the electron range at 15 kV is 0.99 µm.

The different interaction volumes are important for determining what you actually see. For example, it is difficult to only get the chemical composition of a surface layer, since the interaction volume of the x-rays is so large. Secondary electrons are good for examining sample morphology and topology since only the surface generated secondary electrons can be detected.

Because electrons are used for the imaging the sample needs to be electrically conductive. If it is not the surface can become charged and the image will be distorted or can drift during analysis. If the sample is mounted in large amounts of non-conductive material electrical charging of the surface can also be a problem. This effect can be reduced by applying a thin layer of gold or carbon to conduct the electrons away, or by masking most of the surface with conductive copper or carbon tape.

Some SEM-instruments also has the possibility of running in low vacuum mode, where water vapour is let into the specimen chamber. The water will reduce the surface charging, but will result in lower resolution.

3.3.1 SEM instrument

Two different microscopes were used. The first microscope was a HITACHI TM3000 table top microscope, which is fitted with an energy-dispersive detector to detect characteristic x-rays and a backscattering electron detector. This is the microscope used for most of the imaging and for the EDS analysis.

The other microscope was a FEI Quanta 200F, which is fitted with a Everhart-Thornley detector (ETD) which collects secondary electrons, a low field detector (LFD) which collects secondary electrons in low vacuum, a solid state detector (SSD) which collects backscattered electrons and an energy dispersive spectrometer (EDS). This microscope has a higher resolution than the TM3000, and also has the possibility of running in low vacuum mode. It was used in an effort to reduce the drift in the EDS measurements, but the EDS detector of this microscope did not detect any nitrogen from the samples.

3.3.2 SEM sample preparation

The cross section samples were prepared following the procedure for optical microscopy, as described in 3.2.2. The samples where either analysed before the etching step, or the polishing steps where performed again if the sample was already etched.

Since the mounting material is an insulator electrical charging of the surface was a problem. To ensure electrical contact between the samples and sample holder the samples were grinded down from the backside to expose the steel and copper and carbon tape was used to mask part of the surface.

3.4 Transmission electron microscopy

A transmission electron microscope (TEM) can be compared to a visible light microscope, but it uses electrons instead of visible light. As the name indicates, it is the electrons that pass through the sample that is used. This requires electron transparent samples, which requires samples to be very thin (~100 nm). A TEM has a much higher resolution than a VLM, but is significantly more complex and in the case of steel requires a great amount of sample preparation.

The electron beam generates several signals as it interacts with the sample in a similar manner as in a SEM. However, the most used signals in a TEM are the transmitted electrons and characteristic x-rays. The electrons are commonly used for imaging and diffraction, but the can also give chemical data if they are analysed with an electron energy loss spectrometer (EELS). The characteristic x-rays are used to determine chemical composition with an energy-dispersive detector as described in 3.3.

The microscope consists of an electron source, electromagnetic lenses, apertures, detectors and a phosphorescent screen. Photographic film or a CCD-camera is commonly used to record the images. The electron source is either a filament made of a LaB_6 crystal or a hair-pin shaped thread of tungsten (W) or a field emission gun. The emitted electrons are accelerated by an anode with a high electrical potential usually in the range of 100-400keV. Lenses and apertures above the specimen focus the beam and control the illumination of the specimen, while the lenses below the specimen focuses and magnify the image or diffraction pattern. Apertures are used to select which electrons pass and have different uses depending on their position. Figure 3-4 is a schematic overview of the microscope.

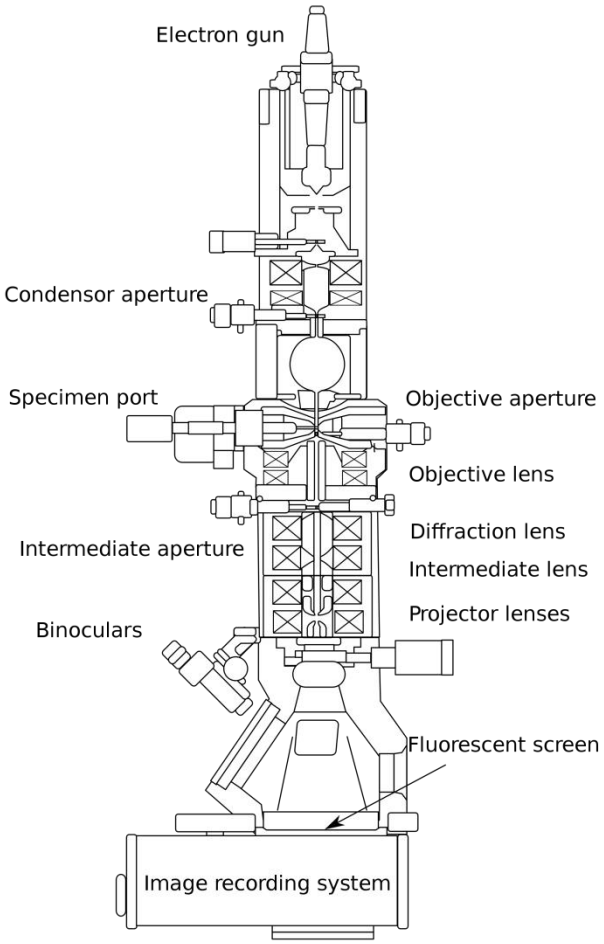

Figure 3-4: Schematic view of a TEM [47]. The intermediate aperture is also called the selected area aperture.

The simplified ray diagram in Figure 3-5 illustrates the electron beams path after it has been scattered in the specimen. Bragg-scattered electrons meet at the same point in the back focal

plane and are forming the diffraction pattern, while electrons scattered from the same point in the sample meet in the image plane and contribute to the image of the specimen.

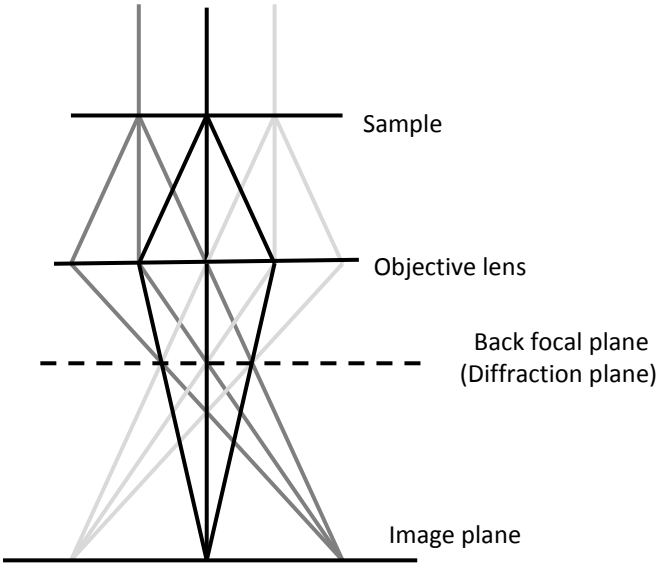

Figure 3-5: Simplified ray diagram in a transmission electron microscope. The objective aperture is placed in the diffraction plane and the selected area aperture is placed in the image plane.

One of the strengths with transmission electron microscopy and electron diffraction is that you can get an image, diffraction pattern and spectroscopy from the same area and this area is typically 1-10 µm, but areas as small as 0.4 µm can be selected. The system of lenses below the image plane in Figure 3-5 can be adjusted to magnify and project either the image or the diffraction pattern illustrated in Figure 3-5. This can be used to analyse the crystal structure of different phases when the grains are in the order of 0.5 µm.

3.4.1 Apertures and imaging techniques

The objective aperture is inserted into the back focal plane to enhance the contrast of the image. If it only let non-scattered electrons (central beam in Figure 3-5) through one get what is called bright field imaging. The beam can also be tilted to only let some of the scattered electrons through the aperture (one of the diffracted beams in Figure 3-5). This is called dark field imaging. Dark field imaging is used to image grains and determine grain size since if the grains are oriented differently they will not scatter at the same angle and this gives contrast in the image.

The selected area aperture is placed in the image plane to limit the area (typically 1-10 µm [41]) contributing to the diffraction pattern. This diffraction data can be used to determine the crystal structure of small grains and thin films as small as 0.4 µm.

If the specimen is illuminated by a parallel electron beam and the area selected with the SAD aperture consists of a single crystalline grain, the diffraction pattern produced will consist of a single diffraction pattern with clear spots, called diffraction spots.

The spots in the diffraction pattern represent planes in the crystal and by measuring the distance between the central beam and the diffracted spots the lattice spacing, d, can be calculated. The relationship between the Bragg angle, θ_B and the distance, R, between the central beam and a spot in the diffraction pattern is given by

$$\frac{R}{L} = tan2\theta_B \approx 2tan\theta_B \approx 2sin\theta_B \quad \textbf{(3-2)}$$

where L is the camera length, which is the effective distance between the specimen and viewing screen. This is illustrated in Figure 3-6.

Combining the Bragg equation (2-10) and equation (2-11) gives the relationship

$$\frac{R}{L} = \frac{\lambda}{d} \rightarrow d = \frac{\lambda L}{R} \quad \textbf{(3-3)}$$

where λL is called the camera constant, K. The camera constant must be calibrated experimentally.

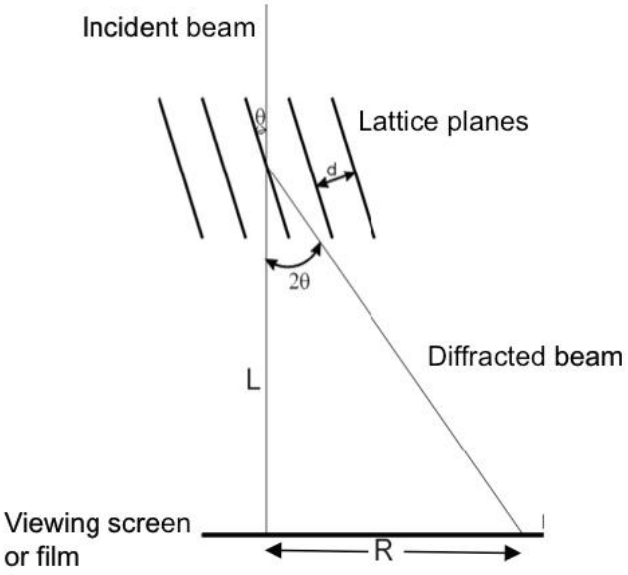

Figure 3-6: Illustration of the relationship between the Bragg-angle, camera length and the distance between the central beam and a diffraction spot [42].

3.4.2 TEM instrument

In the present project a JEOL JEM 2000FX microscope was used. The filament is a LaB_6 crystal and the microscope was operated with an acceleration voltage of 200 kV, corresponding to a wavelength of 0.00251 nm. The EDS detector in the instrument did not work during the experiments.

3.4.3 TEM sample preparation

A good TEM sample can be time consuming to make and needs to fulfil two criteria. It needs large areas that are electron transparent (<100 nm thick) and the sample preparations should not alter the structure or the chemical composition of the sample. There are several different methods to achieve this and in this project ion milling was used. Two different types of samples were aimed to be made: cross section samples to image the compound layer and the diffusion zone of the samples and top view samples.

Ion milling often results in good samples, but is time consuming and the ion milling can change the chemistry of the sample. It is therefore important that the sample is already very thin when ion milling starts. Optimal thickness is below 50 µm and this is achieved by mechanical grinding and polishing.

Top view sample preparation

A piece of the sand blown sample surface were grinded down to about 100 µm using SiC-papers with EFPA grain numbers from 220 to 4000.A disc with 3 mm in diameter was cut out and this disc was further thinned using a Gatan model 656 Dimple Grinder. The specimen is placed on a rotary table, with a rotating grinding wheel conducting the dimpling. The specimen will be thinned more in the middle and less towards the edges. Diamond paste with grain sizes ranging 6 µm to 0.25 µm was used and the thickness of the sample was calculated by measuring the radius, r, of the dimple using the formula

$$d = r^2 D \qquad \textbf{(3-4)}$$

where d is the depth of the dimple and D the diameter of the grinding wheel.

The surface roughness of the sample was a problem during dimpling. Large holes would appear before calculated thickness was achieved. This happened because accurately measuring the starting thickness of the rough surfaced disc was problematic. The thickness was measured with a micrometre and this would measure the maximum thickness of the rough surface. The surface roughness was greater than the wanted specimen thickness and therefore several holes formed before optimum thickness was reached.

None of the samples with a polished surface were used to prepare a top view sample because of time constraints.

Cross section sample preparation

The procedure for making a cross section TEM-sample is time consuming and at each step there is a possibility for the sample to get damaged and if that happens the whole process needs to be repeated.

The sample steel is magnetic and can therefore affect the electrons used for imaging. To limit this effect the goal was to make TEM-samples with as small amount of steel as possible. Figure 3-7 illustrates this goal.

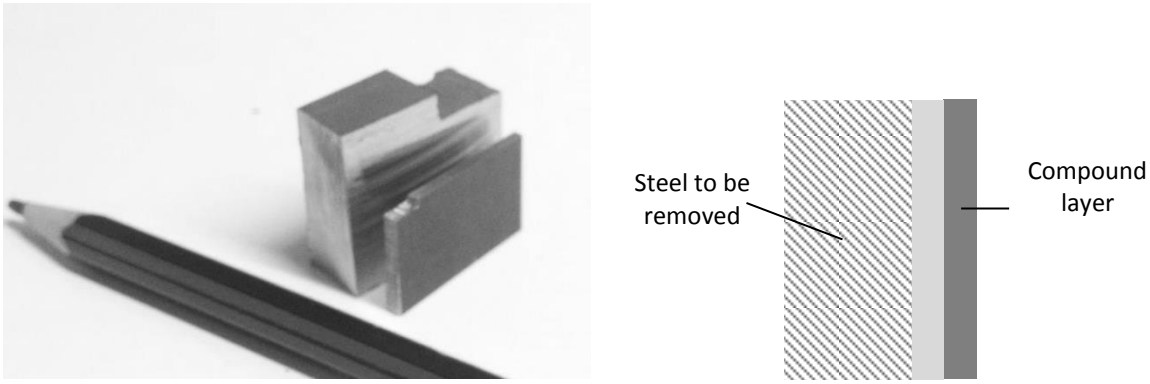

Figure 3-7: To the left a piece of the PPN sample surface after cutting and to the right an illustration of the goal of the thinning process.

About 1 mm of the PPN sample surface was cut off and grinded down to about 100 µm using SiC-papers with EFPA grain numbers from 220 to 4000. Even thickness was difficult to achieve, since the sample bends when thinned which causes the edges to thin more rapidly than the centre. This bending caused the edges to fall off while grinding.

The ~100µ thick foils were cut into 2.5 mm thick strips using a micro diamond saw and strips of glass were glued on to support the sample. The strips were glued together with the surface of interest (PPN) facing each other and supported by glass on each side to obtain a stack of ~3 mm.

The glue first used was Gatan G1, which, in theory, can be hardened in a few minutes using a hot plate. This was not the case, and it often took more than 30 minutes on the hot plate for the glue to harden. The same type of glue from another producer was also used, Allied epoxy bond 110. This glue was also unreliable when considering hardening.

Several samples were lost due to bad glue, and it is important to check the expiry date on the glue, and it is also useful to mix the glue and test its hardening capabilities to ensure the glue is working as intended before gluing together the sample pieces.

The supported sample pieces were then cut into pieces of ~3 mm length. This was done because the TEM sample holder requires samples of 3 mm in diameter. Excess steel is very difficult to remove without a micro saw, and the first group of samples were not cut into 3.1 mm pieces before thinning. This lead to pieces of glass and steel sticking out from the copper ring support, which was glued on before ion milling, and this must be removed to make the sample fit the TEM sample-holder. The glass is very hard and fragile and could easily be

removed by a diamond pen. When trying to remove the excess steel with a diamond pen the whole sample could break, or the steel piece could be ripped off from the copper ring, destroying the sample. The excess steel had to be ground down by keeping the sample between two pieces of glass and carefully removing steel with SiC-paper. This proved very difficult because sthe samples would still break and be destroyed. Cutting the sample stack into pieces of ~3 mm, made the removal of eventual excess steel easier.

The ~3 mm sample stack was thinned again by grinding it down by hand to 50 µm using SiC-papers up to # 4000. A 3mm copper ring with a slot size of 2 mm x 1 mm was glued on for support, and the excess glass and steel was removed. Getting the sample thin enough by hand was not easy, because an unsteady hand would break the sample by thinning it unevenly.

It was found that the safest way to thin the sample to less than 50µm before ion milling was to use the Allied multiprep. This grinding machine uses diamond papers and water to thin the samples while also measuring the thickness for optimal control. This made it possible to aim for a sample thickness of ~20µm. The samples where ground down to 100-150 µm by hand on the SiC-papers before the copper ring was glued on. Then the sample was mounted on the multiprep sample holder and ground down to ~20 µm thickness with diamond papers from 15µm to 1µ grain size. The thickness of the sample was controlled by the micrometer on the multiprep and by visually checking the sample in the light microscope.

The samples are mounted on the multiprep-holder by Crystal bond adhesive, and if more adhesive is used under one part of the sample it can be thinned unevenly. This happened to a few samples. It is also important to check the sample thickness often using the light microscope during the thinning process to ensure the sample is thinned evenly and is not thinned too much and therefore destroyed.

The few samples that survived all the steps in the mechanical thinning process were attempted thinned to electron transparency using an ion mill.

Ion milling

Two ion mills were used. A Gatan Model 691 Precision ion polishing system (PIPS) and Fischione low angle milling and polishing system, model 1010 (Fischione).

For the PIPS Ar^+ ions with energy 5.1 keV were used until a hole in the sample was seen. The angle of the ion-beam was 8° (top) and 6° (bottom). The higher angle on top is to limit sputtering of the copper ring onto the sample. The sample stage was rotating 360°. One sample was ion milled to electron transparency. The process created three holes, one in the middle of the cross-section and to between the glass supports and sample on each side.

For the Fischione Ar^+ ions with energy 5 keV and a current of 5mA was used. The milling angle was 6° and the stage was set to 360° rotation. The sample milled with Fischione was milled for 50 hours without obtaining a hole and because of time constraints the milling of this sample did not finish.

3.5 X-ray diffraction

X-ray diffraction (XRD) gives an average crystal structure and phase composition for a sample. XRD is based on Bragg diffraction and is used to calculate cell-parameters.

X-rays are generated when a filament is heated to produce electrons which are then accelerated in vacuum by a high electric field towards a metal target [48]. The metal is positive and is called the anode. The electron beam will excite the electrons of the metal atoms and x-rays are generated in the relaxation process. The energy levels of the atoms decide the wavelength of the resulting x-rays.

The samples where mounted with the nitride side up, and to know how deep into the sample the x-rays give information from, an estimation of the x-ray penetration depth was calculated for the different angles and wavelengths.

The calculation used Beers-Lambert's law, which relates the absorption of light with the material it travels through [49, 50] .

$$I = I_0 e^{-(\frac{\mu}{\rho})\rho\chi} \qquad \textbf{(3-5)}$$

where I is the transmitted intensity, I_0, the original beam intensity, μ the linear absorption coefficient, ρ the density of the material and χ the thickness of the material. The absorption coefficient for the different nitrides was found by multiplying the nitrogen and iron absorption coefficients with the ratio between the elements in the unit cell. The absorption coefficients wer found in the international tables for crystallography [50].

To find the maximum penetration depth the transmitted intensity was set to 1% and the thickness, χ, was calculated, using a variation of (3-5):

$$\chi = \frac{ln(\frac{I}{I_0})}{-(\frac{\mu}{\rho})\rho} \quad \textbf{(3-6)}$$

The penetration depth is then given as:

$$Penetration\ depth = \sin(\theta) \times \frac{\chi}{2} \quad \textbf{(3-7)}$$

Figure 3-8 illustrates the geometry used in the calculation.

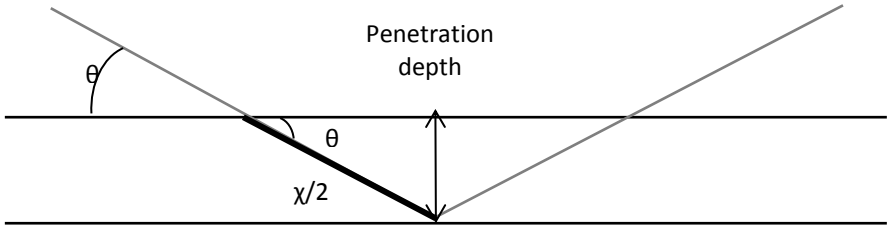

Figure 3-8: Illustration of penetration depth geometry.

Table 3-3 gives the approximate penetration depths for both Mo_α and Cu_α radiation in Fe, Fe_3N and Fe_4N.

Table 3-3: Approximate penetration depth for different angles and wavelengths in Fe, Fe_3N and Fe_4N.

Angle (2θ)	**Fe Mo_α Depth (µm)**	**Fe_3N Mo_α Depth (µm)**	**Fe_4N Mo_α Depth (µm)**	**Fe Cu_α Depth (µm)**	**Fe_3N Cu_α Depth (µm)**	**Fe_4N Cu_α Depth (µm)**
10	0,288	0,383	0,359	0,036	0,048	0,045
30	0,854	1,136	1,066	0,106	0,142	0,133
50	1,394	1,855	1,740	0,174	0,231	0,217
70	1,892	2,518	2,362	0,236	0,314	0,294
90	2,333	3,104	2,912	0,291	0,387	0,363

A normal source of x-rays is copper. When the sample contains iron and the x-rays are generated from a copper source an effect called fluorescence can be observed. The copper-generated x-rays are strong enough to excite the iron atoms and the atoms will then emit x-rays themselves. These x-rays will be detected by the instrument and will become background

noise in the measurement. This effect can cause the reduced penetration depth displayed in Table 3-3.

Fluorescence can be minimized by using x-rays from a different source, like molybdenum, or by applying a filter to the detector. The background can also be subtracted from the resulting diffractogram, but low intensity peaks can be lost.

3.5.1 XRD instrument

Two different instruments were used; an instrument, with monochromatic Cu-$K_{\alpha 1}$-radiation, and an instrument with Mo_{α}.

The resulting diffractograms were analysed using the program EVA and Rietveld refinement with GSAS was performed by Andrey Kosinskiy.

3.5.2 Sample preparation and experimental procedure for XRD

A ~ 1 mm thick slice was cut from the top surface of the PPN samples with the polished surface, PPN with condition 1, 2 and 3. The sample dimensions was 20 x10 x1 mm, and the corners where rounded by grinding with SiC-papers.

The Cu-$K_{\alpha 1}$- radiation measurements where performed from 2° to 90°, with 1 second per collecting point.

The Mo-$K_{\alpha 1}$-radiation measurements where performed from 15° to 85°, with 0.5 seconds per collecting point.

3.6 Hardness measurements

Hardness is a measure of how resistant solid matter is to various kinds of permanent shape change when a force is applied [51]. Hardness can be evaluated in three different ways: scratch hardness, indentation hardness and rebound hardness. In this project indentation hardness has been measured.

Indentation hardness measures the materials resistance to an object pressed against it with a known force. The indenter can have different shapes and gives rise to the different scales of hardness such as Vickers, Brinell, Knoop and Rockwell [52].

The Vickers indenter is diamond shaped and is applied to the material with a set load, measured in kilograms. When the indentation is made, the depth of the indentation can be measured by measuring the diagonals of the diamond shaped mark with a microscope. The length of the diagonals corresponds to a hardness value found in a table. The unit of Vickers hardness measurements is HVX where X is the load in kilograms.

When a material is composed of different grains Vickers measurements can vary. If the diamond shaped indenter hits a very hard particle in the material the resulting indentation will give a smaller diagonal and correspondingly a higher HV value. The larger the indenter is, the more average the result will be for the material.

Hardness measurements with a low applied load are called micro hardness measurements. The indenter of these measurements is in the micrometre range and therefore some variation in the measurements can be expected if the material is made of different phases or grains. Several indentations are needed to give an average picture of the material.

Hardness can be used to evaluate changes in properties in the material, for example hardening depth, and in this project work it is used to measure the diffusion zone depth by finding the depth where the hardness equals 50HV0.2 more than the core hardness of the material [53].

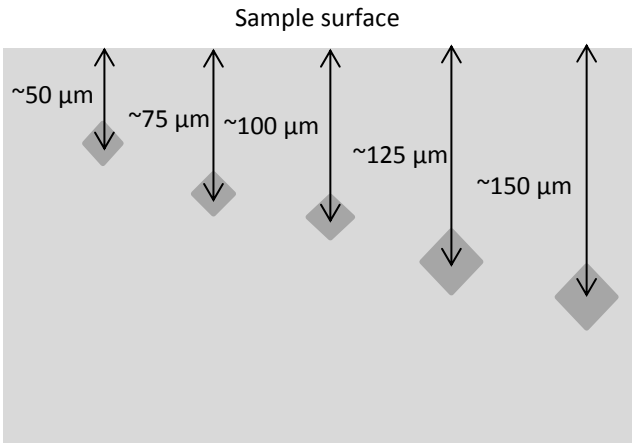

Figure 3-9: Illustration of a series of hardness measurements. The measurements are taken in a series of five indentations, with depth in the sample varying from 50-150 µm.

When measuring the hardness of a cross-section sample in different depths, a hardness profile can be produced. The measurements are taken in a series of five indentations, which are at depths ranging from 50-150 µm, as illustrated in Figure 3-9. The results can then be fitted with a Boltzmann-function and the point where the fitted curve has a hardness that equals 50

HV0.2 more than the core hardness is called the case depth and corresponds to the diffusion zone depth.

3.6.1 Indentation hardness instrument

A Zwick materialprüfung Vickers indenter was used. It is fitted with a VLM to measure the diagonals of the indentation. The uncertainty of the scale for measuring the indentation diagonal is 0.25 µm, but to get a correct reading the sample needs to be in correct focus.

A standard test piece was measured regularly to calibrate the reading of the indentations, but only a test piece for the HV1 scale was available.

3.6.2 Sample preparation for hardness testing

The procedure for VLM-sample preparation was followed, as described in 3.2.2. The samples where either analysed before the etching step, or the polishing steps where performed again if the sample was already etched.

4 Results

4.1 Compound layer and diffusion zone thickness and composition

The compound layer thickness was measured using the VLM and confirmed using SEM. The composition was examined using EDS in the SEM. The compositional analysis by the EDS only gives percentage of elements, so the distribution could not be determined.

4.1.1 Rough surface sample, PPN condition 1

1-Rough (PPN under condition 1) has an uneven white surface region, which is missing in some parts, as can be seen in the images in Figure 4-1. The white region is the compound layer, and it measures between 1.2 and 2.3 µm, as can be seen in Figure 4-2. The steel is etched, which reveals a martensitic microstructure and the white compound layer.

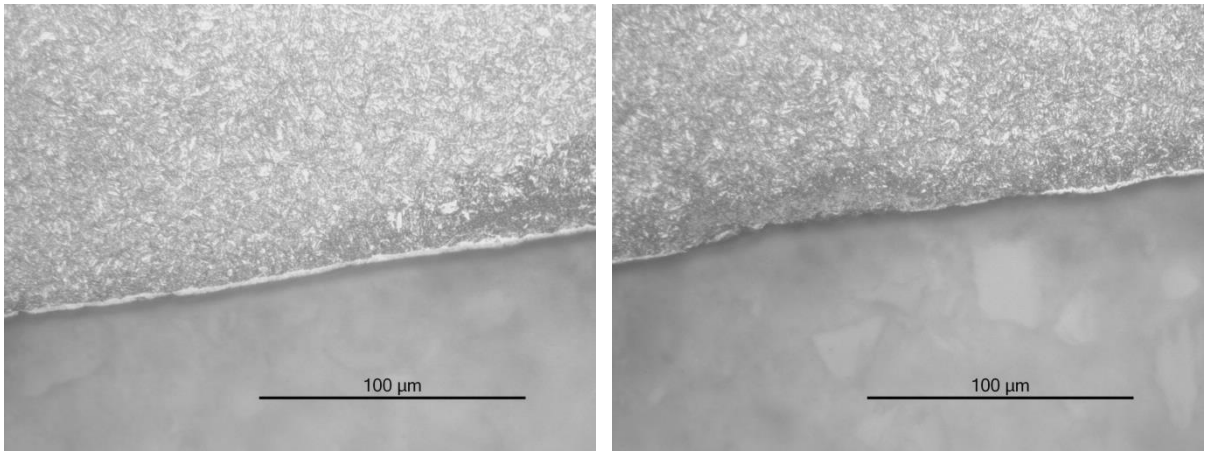

Figure 4-1: VLM overview images of 1-rough. The sample is at the top of the images. The nitride layer is fairly uneven, as can be seen to the left, and in some regions completely gone, as can be seen to the right.

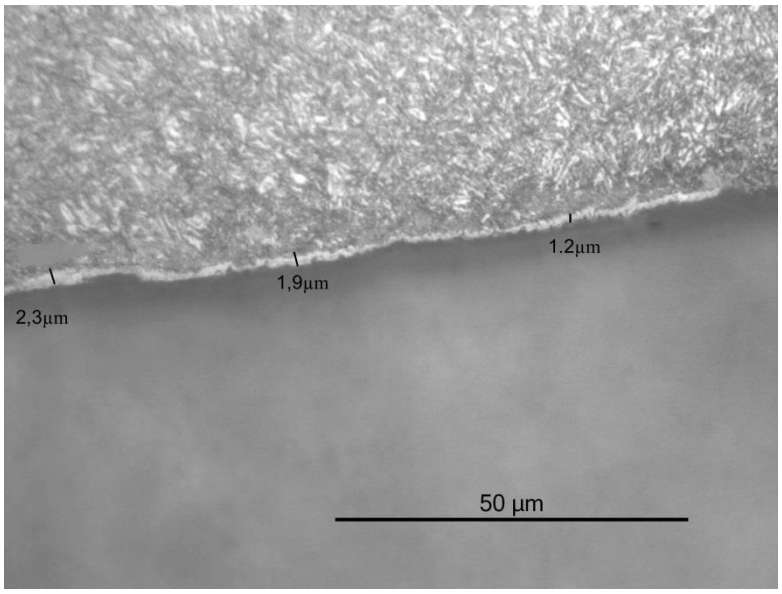

Figure 4-2: VLM image of 1- rough. The sample is at the top of the image. An uneven, white surface region can be seen, which measures between 1.2 µm and 2.3 µm.

Analysis in SEM shows a slightly darker surface region of about 2 µm, Figure 4-3. The thickness and uniformity correlates to the VLM images in Figure 4-1 and Figure 4-2. The sample is not etched and is to the right in the images. While the contrast in the VLM comes from light reflected of an etched surface, the contrast in the SEM image is made by the different elements interacting with the electron beam. The steel consists of about 97% iron and the heavy iron cores creates more BS-electrons than the lighter aluminium, silicone and oxygen atoms in the mounting material. This makes the sample appear white and the mounting material dark.

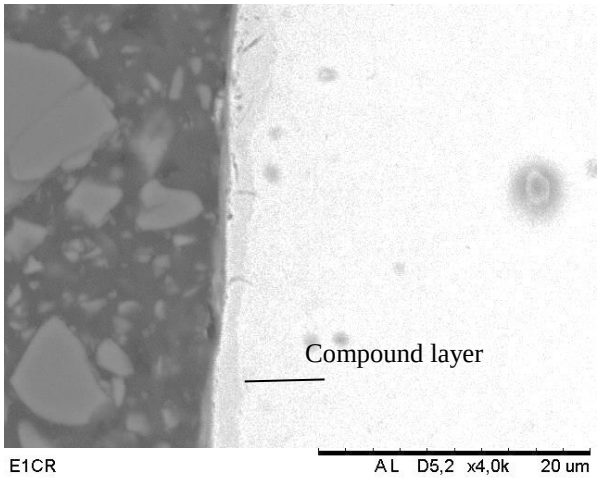

Figure 4-3: SEM image of 1-rough. The sample is to the right in the images. A thin surface region can be seen, of about 2 µm thickness.

Compositional analysis with EDS shows a higher concentration of nitrogen in the darker surface region, as can be seen in Figure 4-4, which is consistent with a compound layer on the surface.

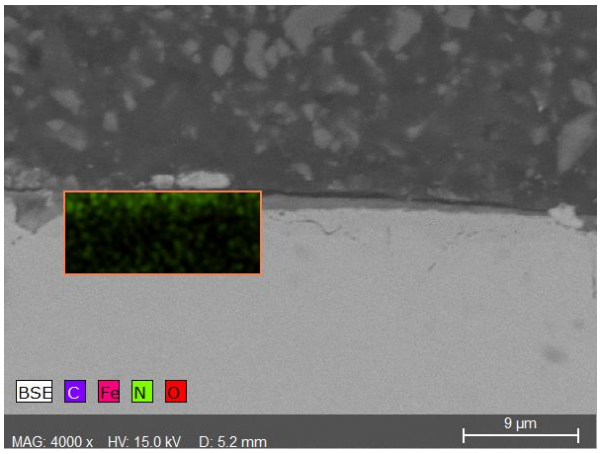

Figure 4-4: Element map of nitrogen of 1-rough. The sample is at the bottom of the images.

4.1.2 Smooth surface sample, PPN condition 1

Figure 4-5 shows a VLM overview image sample 1-smooth. This sample is nitrided with the same parameters as 1-rough, but without the oxidizing step at the end. The thin bright region on the steel surface is consistent with the nitride compound layer, while the steel shows a martensitic structure. The sample is at the top side of the images. As can be seen from Figure 4-5 the compound layer has an even thickness with t= 2.3 and 2.4 µm. Some occasional cracks as can also be seen

The cracks in the surface layer are most probably caused by the sample preparation. The thickness of the compound layer is similar to the compound layer thickness of the rough surface sample, but the layer in the smooth sample is much more uniform.

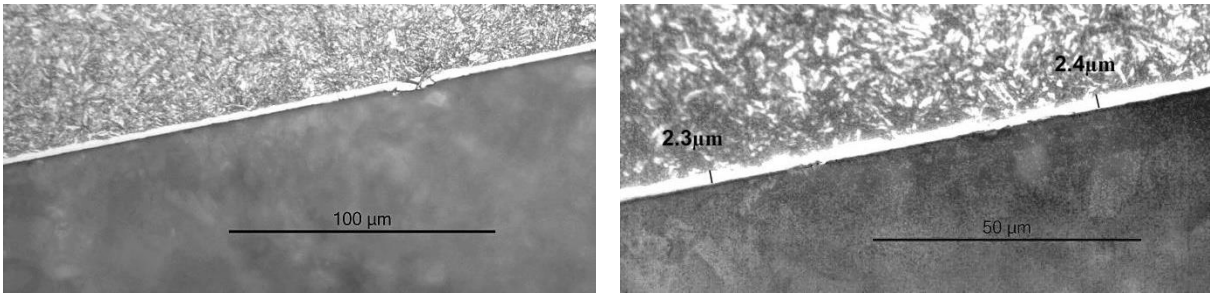

Figure 4-5: VLM image of 1-smooth. The sample is at the top side of the images. The bright region on the steel surface is the compound layer. The measured thickness is 2.3 µm and 2.4 µm.

Figure 4-6 shows a surface region from 1-smooth imaged with SEM. The thickness of the compound layer is found to be about 2 µm and in agreement with the observations made by VLM. The sample is to the right in the images. The surface shows some evidence of cracks and pieces of the surface region is chipped off.

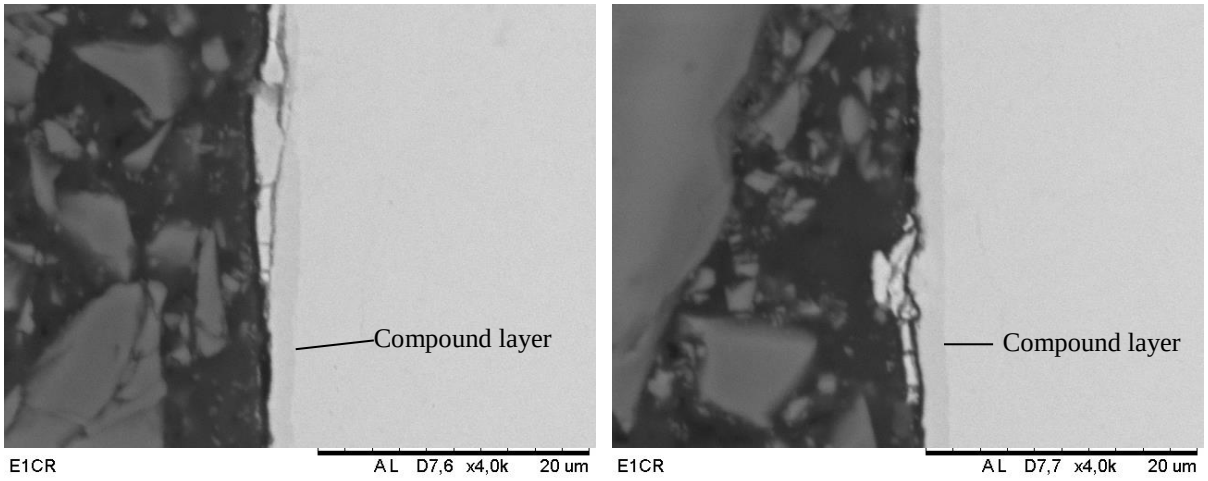

Figure 4-6: SEM 1-smooth. A 2 µm thick surface region can be seen. The sample is the grey region to the right in the images.

EDS analysis of the sample show a slightly higher concentration of nitrogen at the edge of the sample. An element map of nitrogen, which can be seen in Figure 4-7, shows a surface region with more nitrogen, while the element map of oxygen does not show this higher surface concentration.

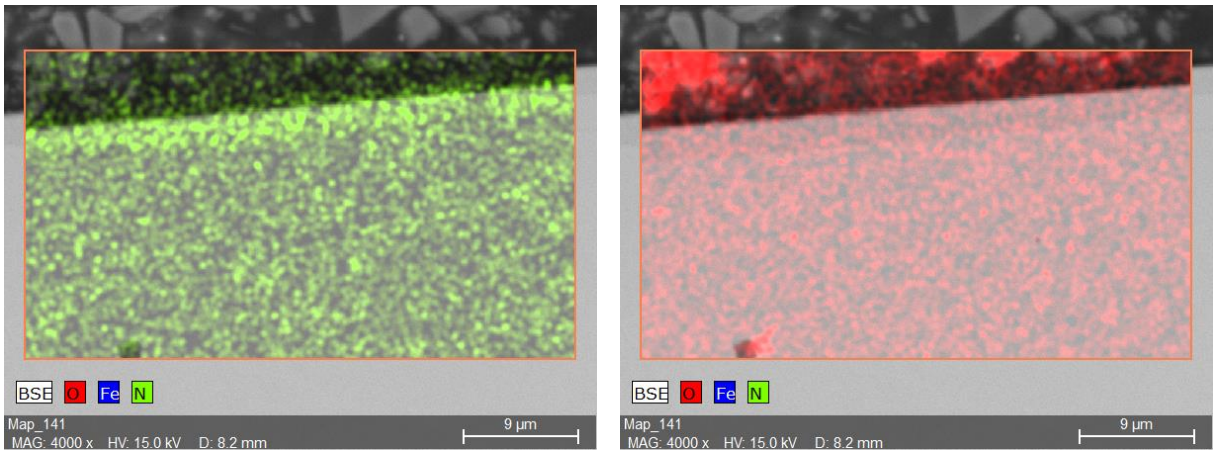

Figure 4-7: Element map showing nitrogen and oxygen in smooth- 1. Green represents nitrogen and a higher concentration can be seen at the surface, while red represents oxygen where no increased concentration can be seen on the surface.

EDS analysis also shows a gradually lower amount of nitrogen further away from the surface, as can be seen in **Error! Reference source not found.** and Table 4-1.The results are normalized to only include iron, nitrogen, oxygen and chromium. The measuring points closer to the surface gives a higher concentration of nitrogen than the measuring points further away from the surface, consistent with the assumption of a diffusion zone with decreasing nitrogen after the compound layer. As can be seen in **Error! Reference source not found.** the sample image drifts during signal collection.

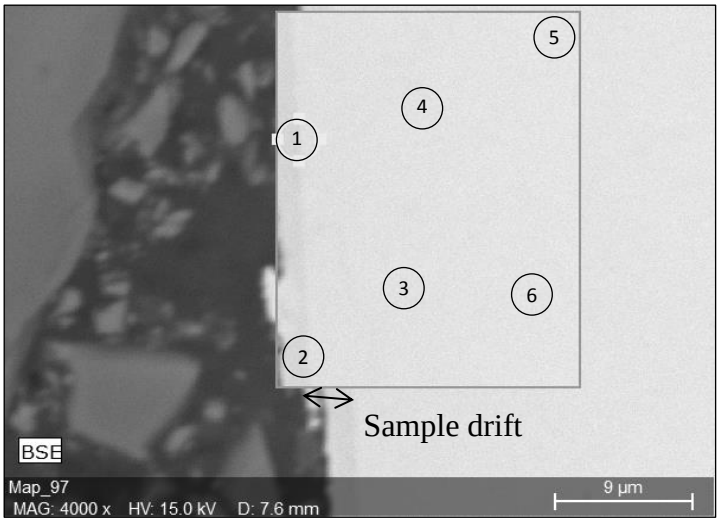

Figure 4-8: Analysis area for chemical composition. The image drifts during collection.

Table 4-1: Element analysis using EDS. The percentages are normalized to include only iron, oxygen, nitrogen and chromium.

	Distance from surface (µm)	Norm. at% Iron	Norm. at% Nitrogen	Norm. at% Oxygen	Norm. at% Chromium	Total
1	0-2	70.8	11.2	17	1	100
2	0-2	78.9	6.7	13.4	1	100
3	7-9	96.3	2.3	0.7	0.7	100
4	8-10	95.7	3.1	0	1.1	100
5	16-18	95.9	0.8	2.1	1.2	100
6	15-17	95.6	0.2	3.1	1.1	100

4.1.3 PPN condition 2, the low temperature treatment

Figure 4-9 shows a VLM overview image of 2- Low T. This sample is PPN with the low temperature process and normal plasma. The sample is on the bottom side of the images. As can be seen from Figure 4-9 the compound layer is uneven and thickness ranges from t= 1.0 to t=1.9 µm. Some places the nitride compound layer has expanded into the steel, indicating surface impurities or contamination.

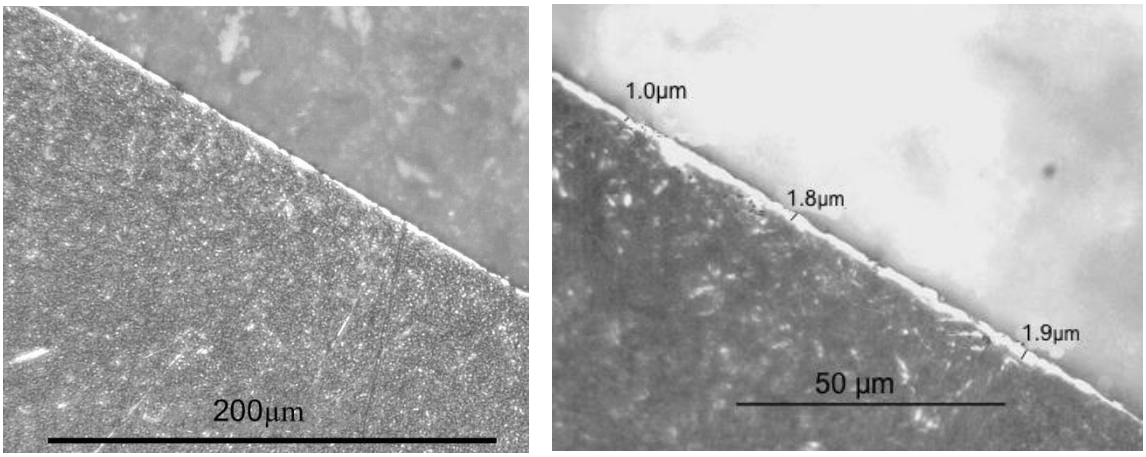

Figure 4-9: VLM images of 2-Low T. The sample is on the bottom left of the images. The bright region on the steel surface is the compound layer. The measured thickness is 1.0 µm, 1.8 µm and 1.9 µm.

Figure 4-10 shows a surface region from 2- low T imaged with SEM. The thickness of the compound layer is found to be less than 2 µm and is in agreement with the observations made by VLM. The sample is to the left in the image. One of the images is taken in low-vacuum

mode to decrease surface charging and to obtain greater resolution. The sample imaged in low-vacuum has been etched with Nital.

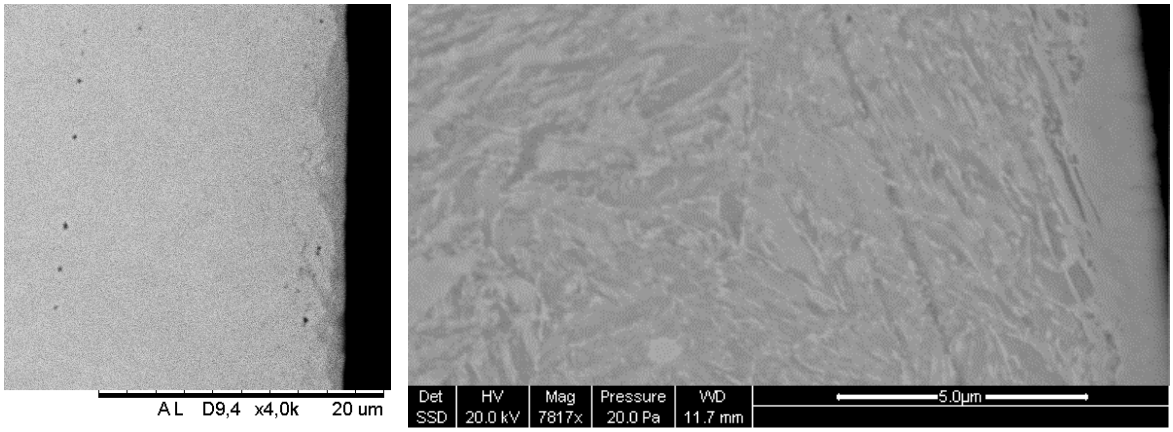

Figure 4-10: SEM-image of 2-low T. A surface region of less than 2 µm can be seen. The right image is taken in low- vacuum mode and is of a heat treated and etched 2-low T sample, so the microstructure of the steel is visible.

EDS analysis of 2-low T show a slightly higher concentration of nitrogen at the surface. An element map of nitrogen, which can be seen in Figure 4-11, shows a surface region with more nitrogen, while the element map of oxygen does not show this higher surface concentration

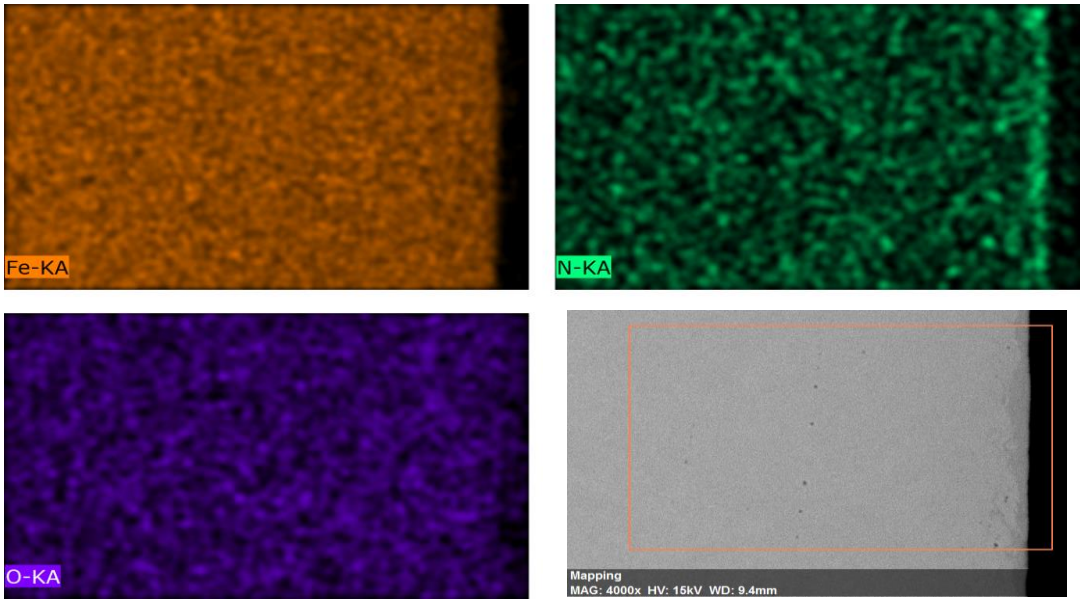

Figure 4-11: Element map of 2-Low T. A slightly higher concentration of nitrogen (green) can be seen on the surface, while there is no increased oxygen (prurple) concentration. The orange is iron.

4.1.4 PPN condition 3, the no compound layer sample

Figure 4-12 shows a VLM image of sample 3 – No CL. This sample is PPN with the low temperature process and diluted plasma. The goal of the PPN was to make a sample with no compound layer, but with a diffusion zone. As can be seen in Figure 4-12 a thin white surface region with a thickness of t=0.2 and t=0.3 µm is present. The compound layer is uniform and even.

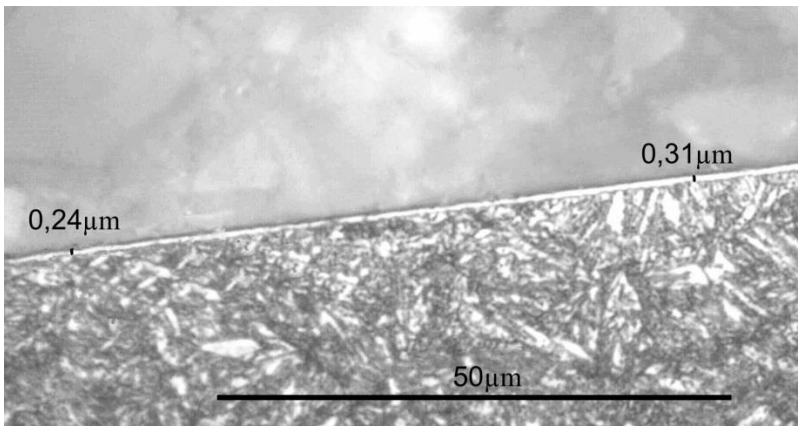

Figure 4-12: VLM image of 3 – No CL. The bottom part of the image is the sample. The bright region on the steel surface is the compound layer. The measured thickness is 0.2 µm and 0.3 µm

Figure 4-13 is a SEM-image of 3 - No CL and shows a slightly darker surface region with a thickness of less than 1 µm thick, consistent with the VLM image in Figure 4-12.

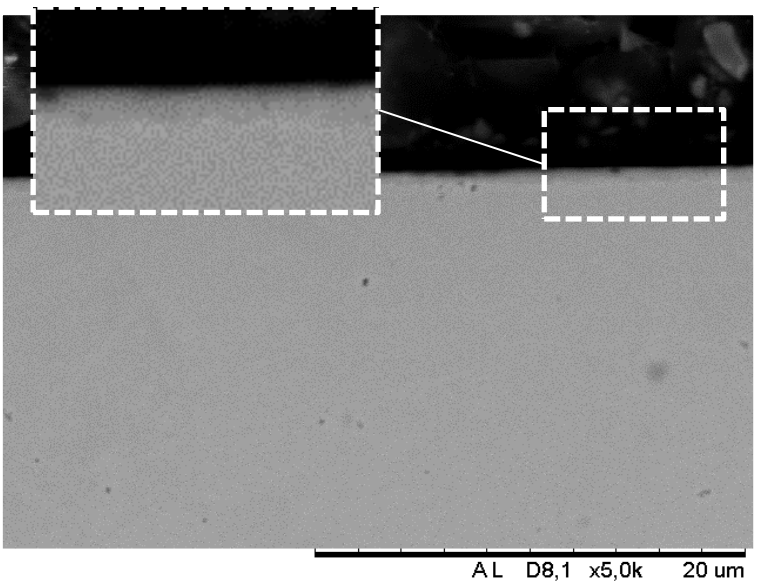

Figure 4-13: SEM image of the sample PPN under condition 3. A slightly darker surface region of less than 1 µm can be seen. The sample is at the bottom of the image.

An element map of iron, nitrogen and oxygen is presented in Figure 4-14. This shows a slightly higher concentration of nitrogen at the surface of the sample, but no higher concentration of oxygen. This is consistent with a thin compound layer at the surface.

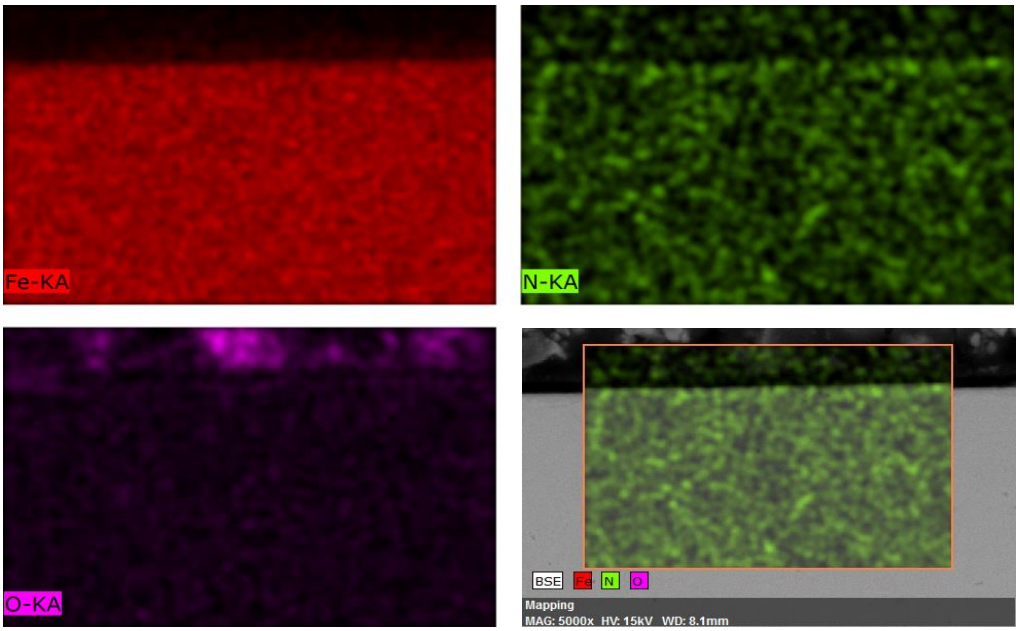

Figure 4-14: Element map of 3 - No CL. A higher concentration of nitrogen (green) can be seen on the surface, while no higher surface concentration of oxygen (pink) is observed. Red is iron.

The concentration of nitrogen was measured by EDS spot analysis at 6 different positions as indicated in Figure 4-15. The results in Table 4-2 are normalized to make oxygen, nitrogen, chromium and iron total at 100%. The results show gradually lowering of the concentration of nitrogen deeper into the sample, consistent with a diffusion zone with decreasing amount of nitrogen. The sample image drifted during the measurement.

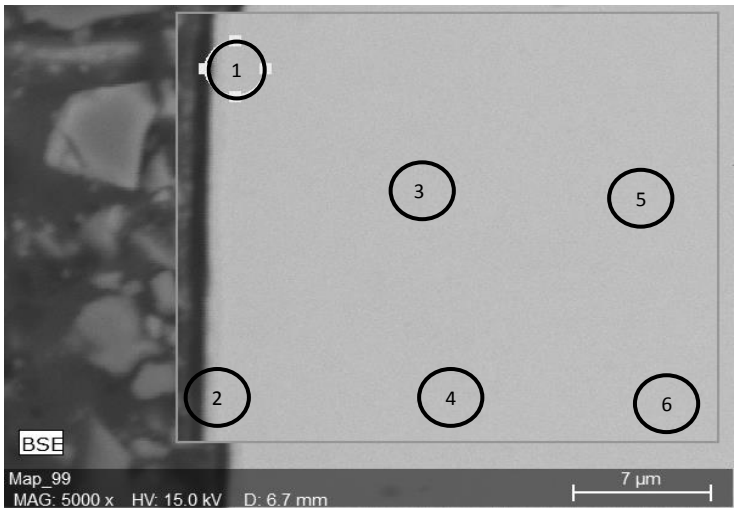

Figure 4-15: Analysis area for chemical composition of 3- No CL. The sample image drifted druing the collection.

Table 4-2: Element analysis using EDS for sample nitride under condition 3. The percentages are normalized to include only iron, oxygen, nitrogen and chromium.

	Distance from surface (µm)	**Norm. at% Iron**	**Norm. at% Nitrogen**	**Norm. at% Oxygen**	**Norm at% Chromium**	**Total**
1	0-3	79.2	7.9	12.3	0.6	100
2	0-3	83.4	7.1	8.8	0.7	100
3	10-13	94.5	1.1	3.4	1.1	100
4	12-15	94.1	3.6	1.4	1.0	100
5	22-25	98.2	0.9	0.00	0.9	100
6	24-27	97.0	1.8	0.00	1.2	100

4.2 Diffusion zone thickness and composition

The diffusion zone thickness was calculated with hardness measurements, as described in 3.6. One set of samples were also heat treated to get the nitrogen to precipitate out of the solid solution, but the martensitic structure of the steel made the growth of nitride needles impossible to see when etching with Nital.

4.2.1 Rough surface sample, PPN condition 1

Figure 4-16 shows the hardness measurements done on 1-rough. Four series of measurements where done, on four different parts of the sample. It can be seen that some of the series are

lower in hardness overall, but the shape of the curve remains similar between all the series. This discrepancy indicates a large uncertainty in the measurements. The diffusion zone was measured to be between 125 µm and 140µm, with an average of 138 µm when all the data points were used in the Boltzmann-fit of the curve.

The hardness of the sample before nitriding was measured to be 388 HV0.2, and the measured core hardness of 1- rough was 396 HV0.2. This indicates that the nitriding process has not changed the core hardness significantly. The surface hardness was measured to 781 HV1, since the rough surface is difficult to measure using HV0.2.

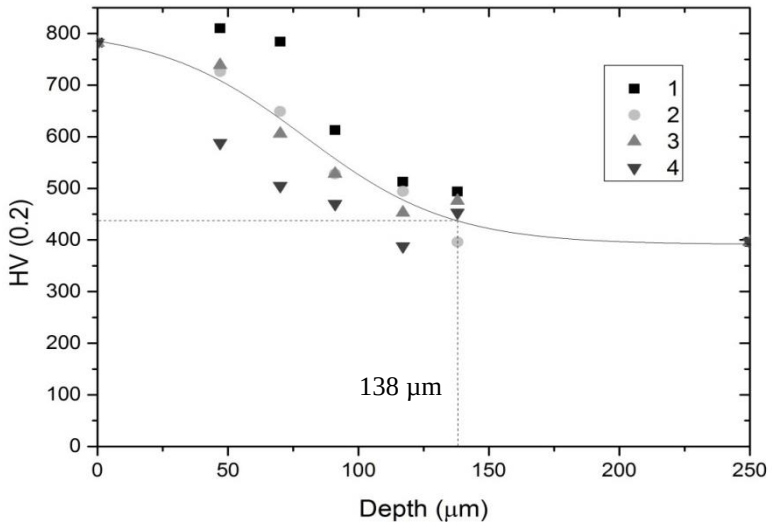

Figure 4-16: Hardness measurements for 1-rough. Four series of measurements where done and the average case depth is 138 µm.

4.2.2 Smooth surface sample, PPN condition 1

Figure 4-17 shows the hardness measurements done on 1-smooth. Five series of measurements where done, on five different parts of the sample. Again it can be seen that some of the series are lower in hardness overall, but the shape of the curve remains similar between all the series. This indicates a large uncertainty in the measurements. The diffusion zone was measured to be between 100 µm and 175µm, with an average of 131 µm when all the data points were used in the Boltzmann-fit of the hardness profile.

The average case depth corresponds to the case depth found for 1-rough, although a lower core hardness of 345 HV0.2 was found. This lower hardness could be due to uncertainty of the measurements. The surface hardness was measured to be 733 HV0.2.

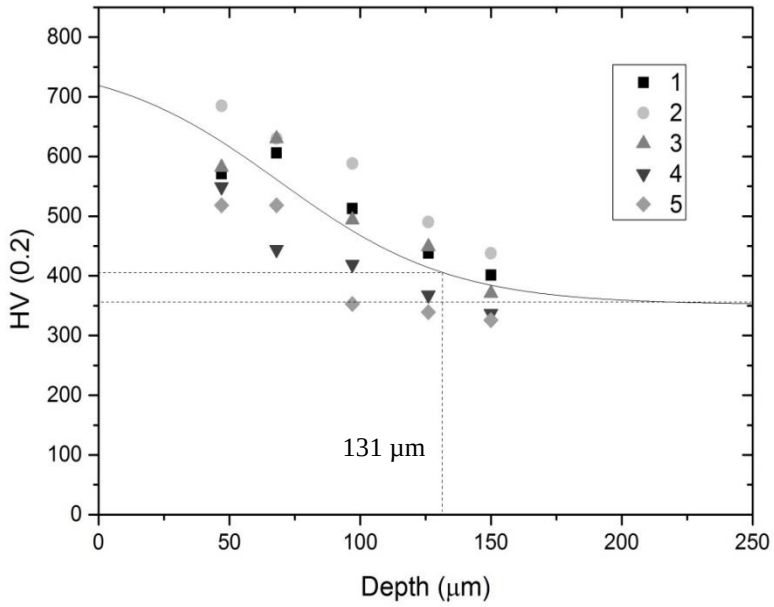

Figure 4-17: Hardness measurements for 1-smooth. Five series of measurements were done and the case depth is approximately 131 µm.

Some of the series had more deformation at the measuring points, maiking it harder to acurately measure the size of the indentation, as is illustrated in Figure 4-18. This deformation difference can explain some of the irregularities of the hardness profile measurements.

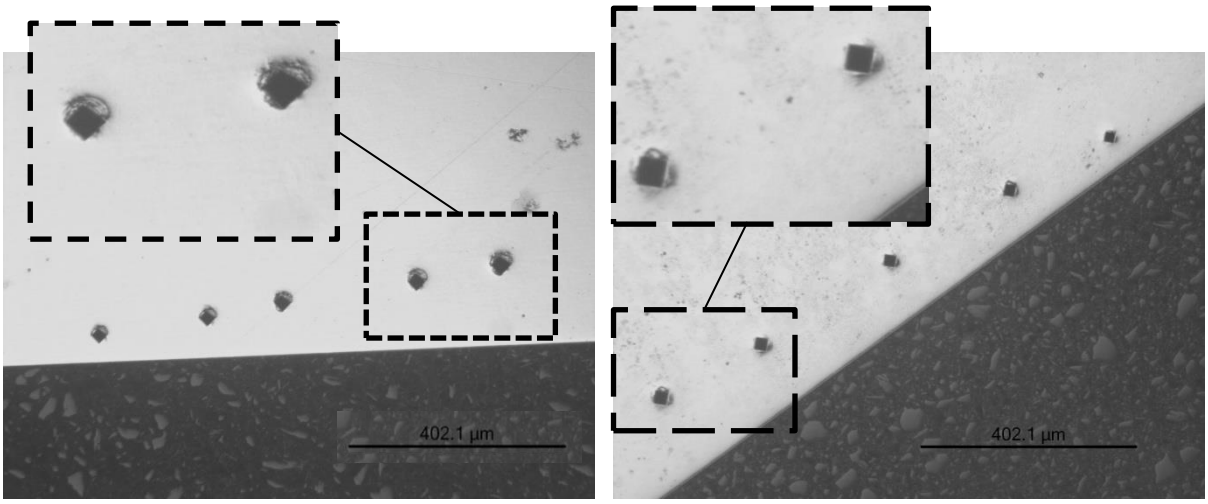

Figure 4-18: Hardness measurement indentations in 1-smooth. The image to the left shows evidence of deformations in the indentations, the image to the right have much less deformation.

4.2.3 PPN condition 2, Low temperature treatment

Figure 4-19 shows the hardness measurements done on 2-Low T. Eight series of measurements where done, on eight different parts of the sample. The diffusion zone was

measured to be between 45 µm and 100µm, with an average of 62 µm when all the data points were used in the Boltzmann-fit of the hardness profile. One of the measurement series yielded a result with significantly higher hardness values than the other measurements series, but the rest of the measurements were fairly consistent.

The core hardness was measured to 365 HV0.2, but the hardness measurements yielded several indentations lower than the core hardness. Based on those measuring points the core hardness was recalculated to 350 HV0.2, which is the hardness used in the plot below. The surface hardness was found to be 788 HV0.2.

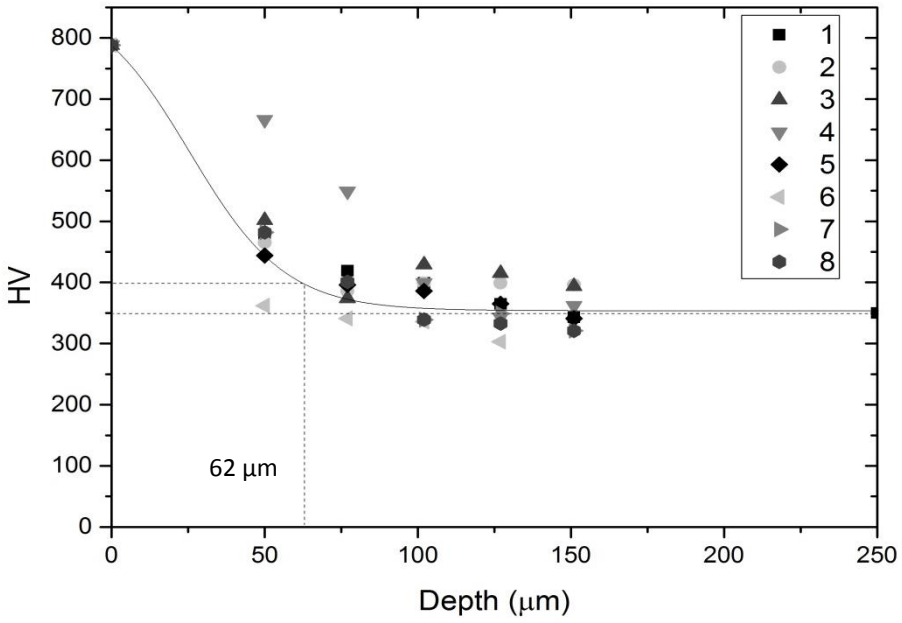

Figure 4-19: Hardness measurements for 2 - Low T. Eight series of measurements were done and the case depth is approximately 62 µm.

Some of the measurements had very deformed indentations, which made it very difficult to accurately measure the indentation size. These results are not included in the above plot, and a typical deformed indentation is presented in Figure 4-20.

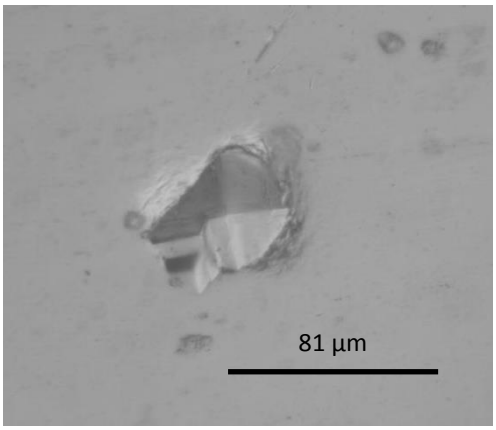

Figure 4-20: A deformed measuring point in 2 – low T. The size of the indentation is difficult to measure.

4.2.4 PPN condition 3, the no compound layer sample

Figure 4-19 shows the hardness measurements done on 3 - no CL. 13 series of measurements where done on 13 different parts of the sample. The sample was uneven so a larger number of series were measured to confirm the results. The diffusion zone was measured to be 106 µm. The core hardness of the sample was measured to be 329 HV0.2 and the surface hardness was 707 HV02.

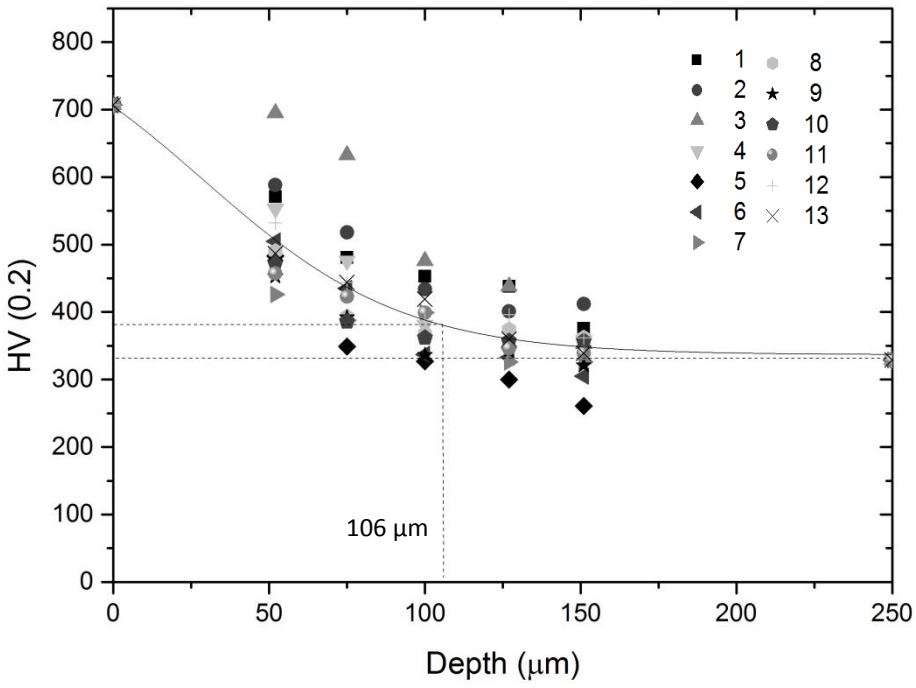

Figure 4-21: Hardness profiles for 3 – No CL. 13 series of measurements were done and the case depth was found to be 106 µm.

4.3 General structure of the compound layers and diffusion zones

XRD was performed on the three samples with polished surface, 1-smooth, 2-low T and 3-No CL. XRD gives an average view of the crystal structure and the calculations in Table 3-3 gives the approximate penetration depths for the x-rays. In most of the cases it can be assumed that the x-rays penetrate past the compound layer of the sample. Both Cu_{α}- and Mo_{α}-radiation was used, but because the XRD data is used to give general indication of which phases are present in the sample, only the Mo_{α}-results are presented.

4.3.1 PPN condition 1, smooth surface

Figure 4-22 shows a diffractogram of 1-smooth. The peaks can be assigned to Fe_3N, Fe_4N and α-iron.

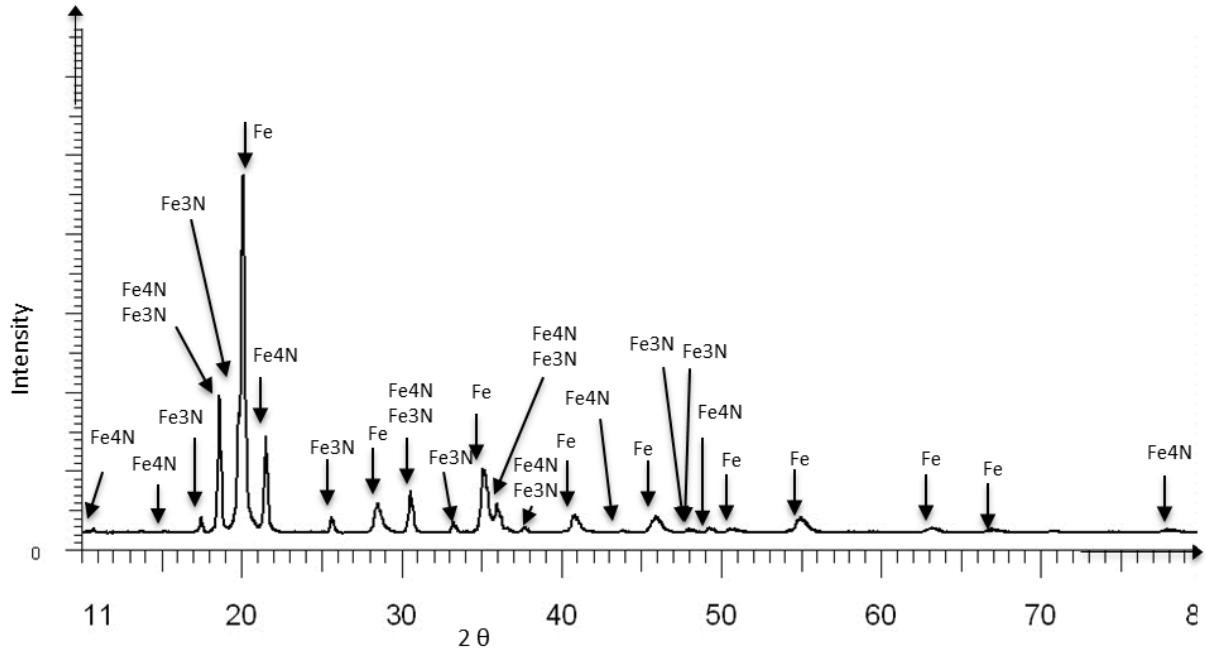

Figure 4-22: Diffractogram obtained from 1-smooth. The different peaks are labelled with the corresponding phase. Both Fe_3N and Fe_4N are present in the sample.

Rietveld refinement of the XRD-result was performed by Andrey Kosinskiy using GSAS to determine the lattice parameter for the iron. Figure 4-23 shows the resulting refinement. The blue line represents the difference between the refined result and the collected data. The

refinement is generally a good fit, but around the two strongest iron peaks the refinement is not a perfect fit. The lattice parameter of the iron was found to be 2.868 Å.

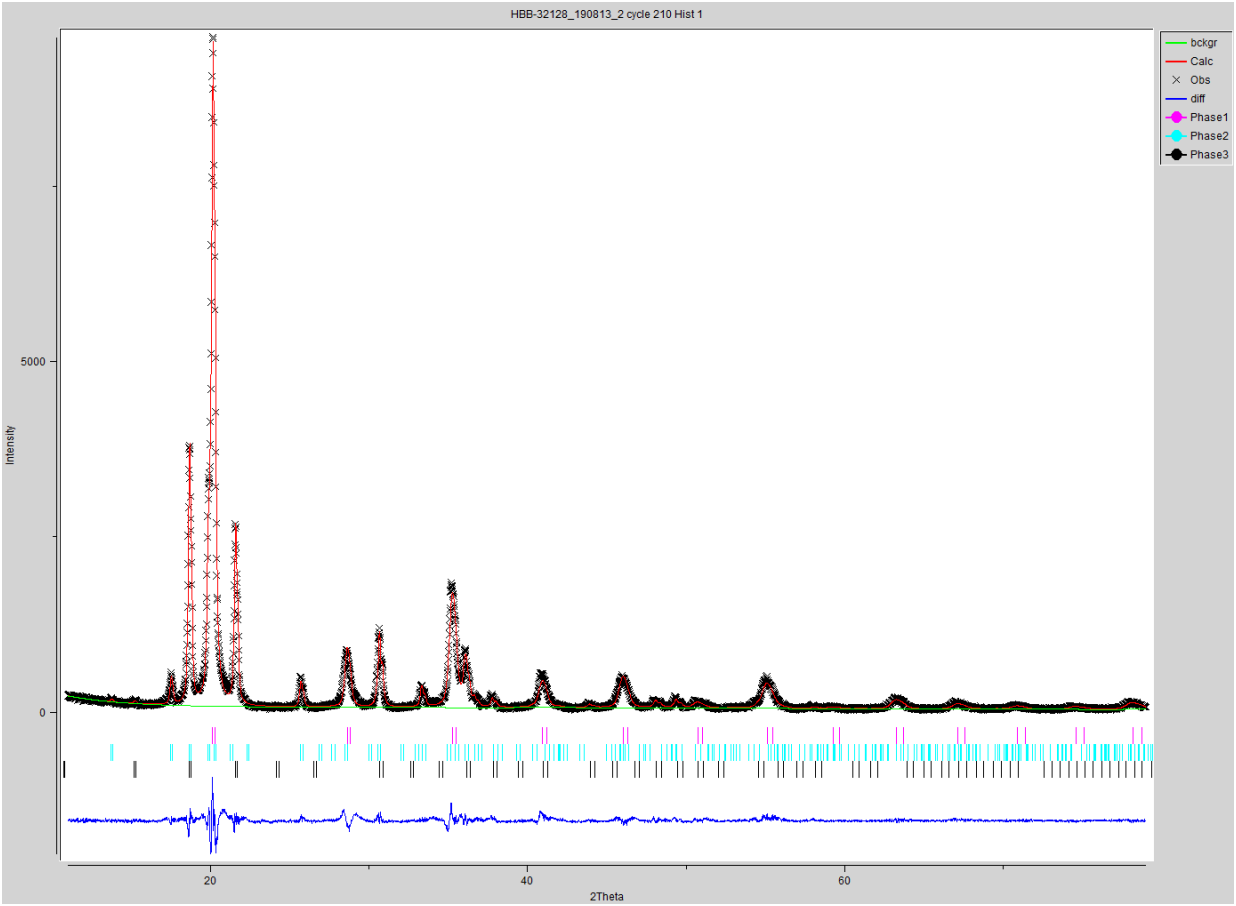

Figure 4-23: Rietveld refinement of the XRD-data for the 1-smooth. Performed by Andrey Kosinskiy with GSAS.

4.3.2 PPN condition 2, Low T

Figure 4-26 shows a diffractogram of 2-Low T. The peaks can be assigned to Fe_3N, Fe_4N and α-iron. This diffractogram has lower intensities of the iron nitride peaks than the 1- smooth diffractogram.

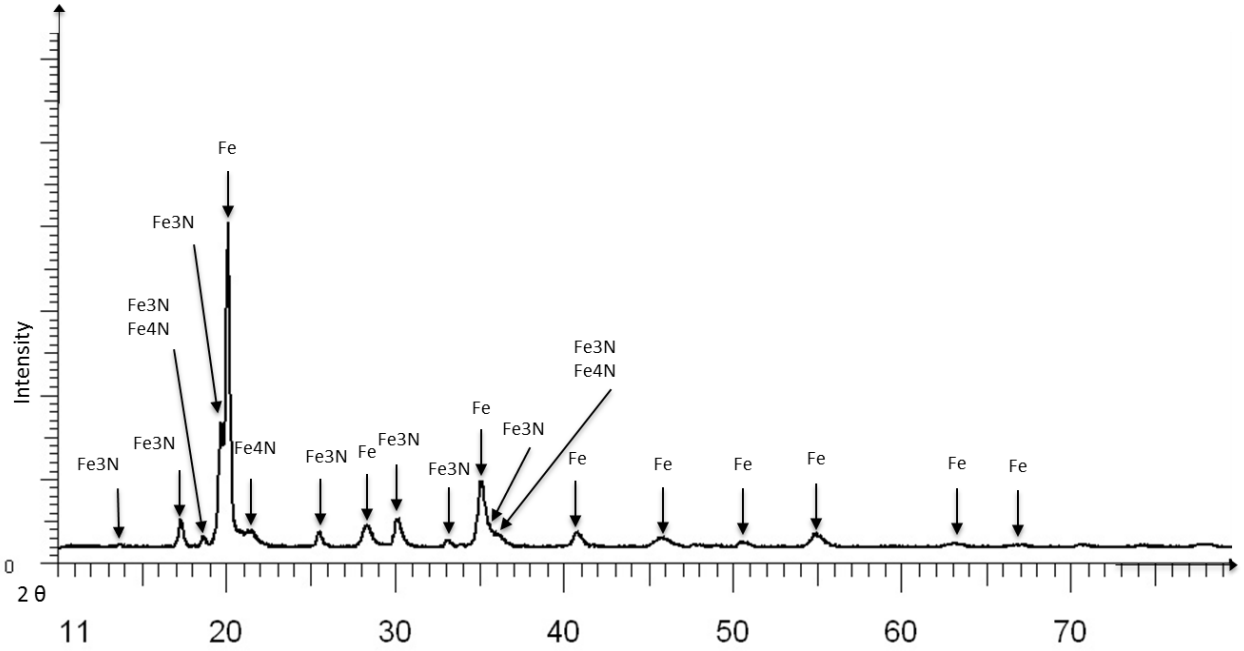

Figure 4-24: Diffractogram obtained from 2-low T. The different peaks are labelled with the corresponding phase. Both Fe_3N and Fe_4N are present in this sample.

The Rietveld refinement of the XRD results, presented in Figure 4-25, gave a lattice parameter for the iron of 2.864 Å. The iron peak at 28° 2θ displays a significant difference between the refined result and the collected data and the Fe_4N peak at 22° 2 θ shows signs of preferential orientation.

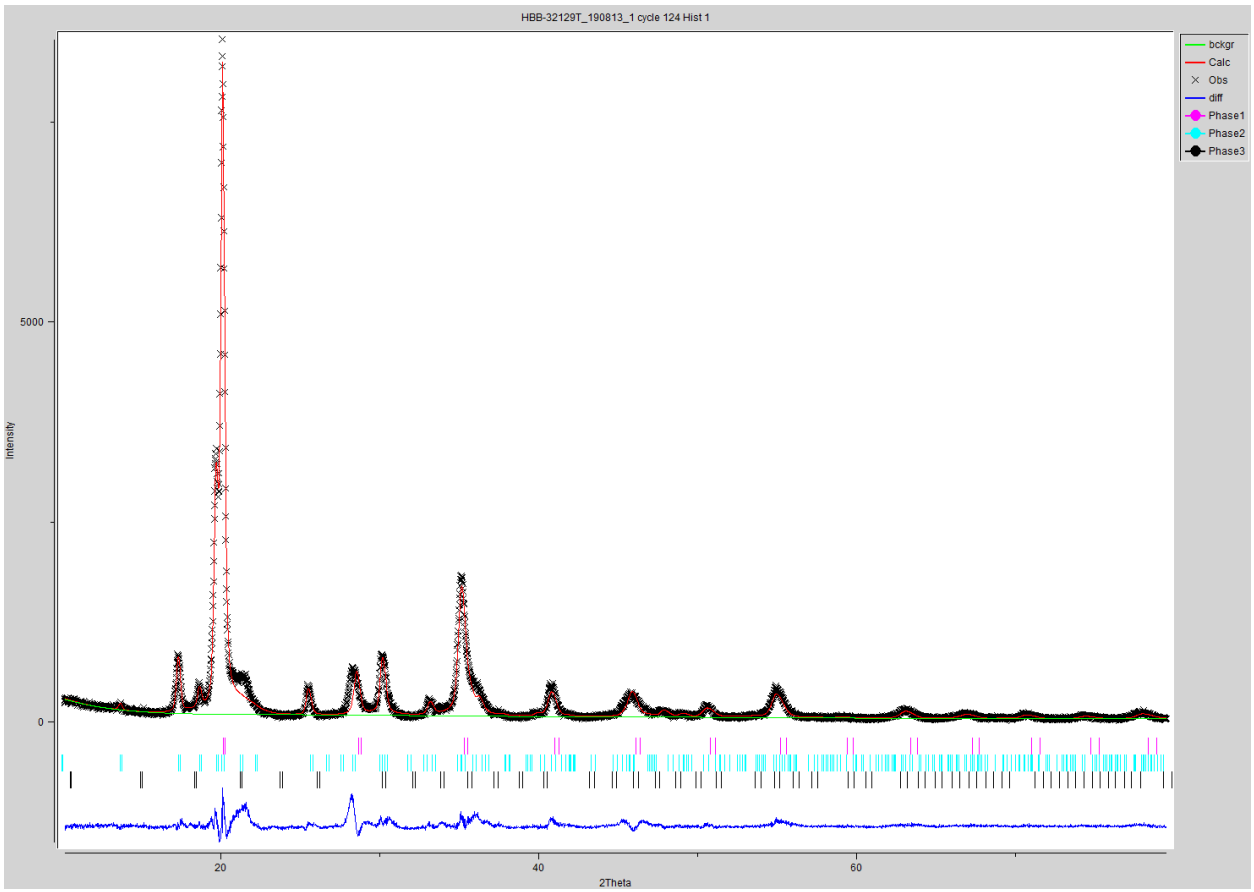

Figure 4-25: Rietveld refinement of the XRD-data for the 1-smooth. Performed by Andrey Kosinskiy with GSAS.

4.3.3 PPN condition 3, no CL

Figure 4-26 shows a diffractogram of 3 – No Cl.The peaks can be assigned to Fe_3N, Fe_4N and α-iron. This diffractogram has lower intensities of the iron nitride peaks than the 1- smooth diffractogram. Rietveld refinement yielded an iron lattice parameter of 2.854 Å.

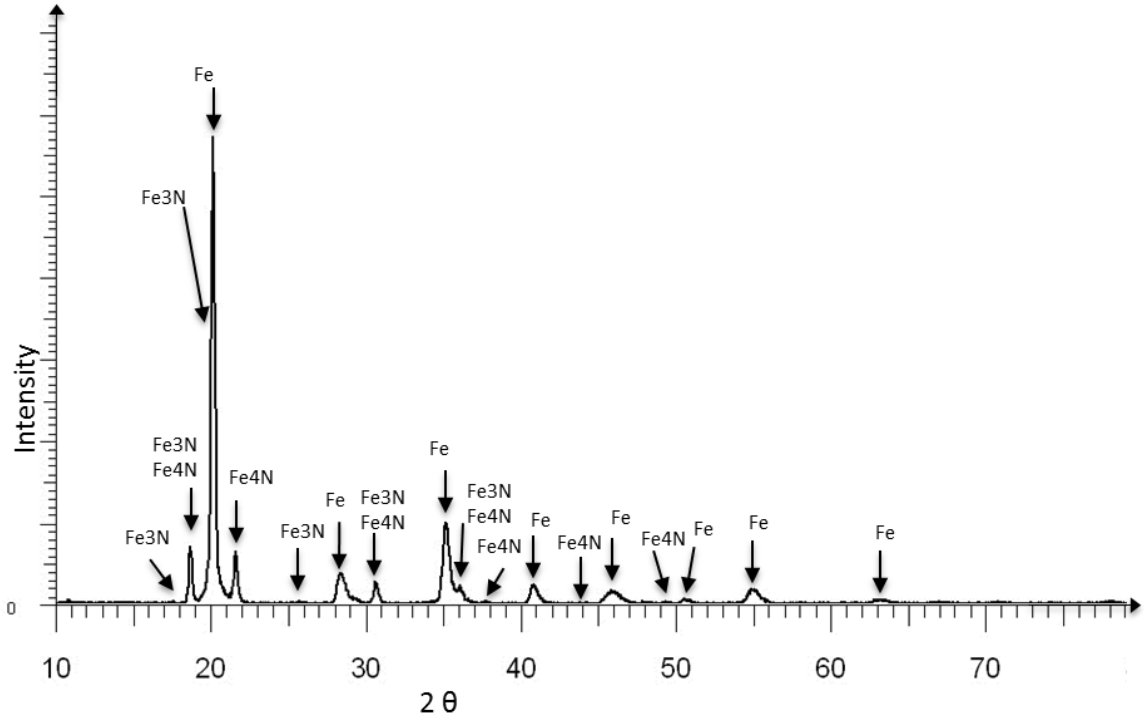

Figure 4-26: Diffractogram obtained from 3-No CL. The different peaks are labelled with the corresponding phase. Both Fe_3N and Fe_4N are present in this sample.

4.3.4 TEM-imaging and electron diffraction

Because of problems with sample preparation and time constraints only 2- low T was analysed with TEM, and only preliminary studies where done. Elemental analysis could not be performed because the instruments EDS-detector was not working at the time of ana

Figure 4-27 is a collection of dark field images from the compound layer of the sample. The images show a varying grain size. Two large grains have been measured to about 200 and 400 nm, but smaller grains appear to be present.

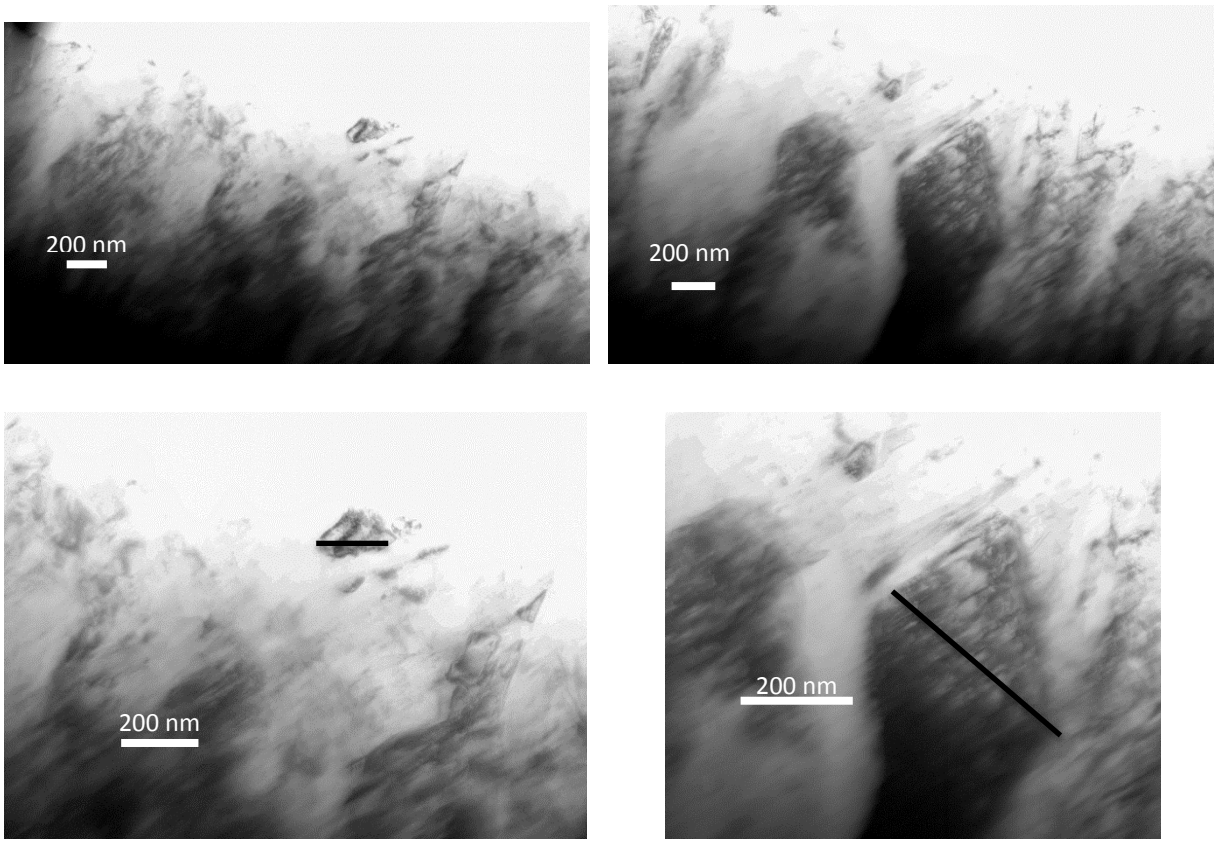

Figure 4-27: TEM images of 2 – Low T taken at 200 kV. In these mages the grain size varies from ~200 nm to ~ 400 nm.

Diffraction with a SAD-aperture from the compound layer was also performed and Figure 4-28 shows one of the obtained diffraction patterns. The smallest aperture was used so the area contributing to the diffraction pattern was about 0.5 μm.

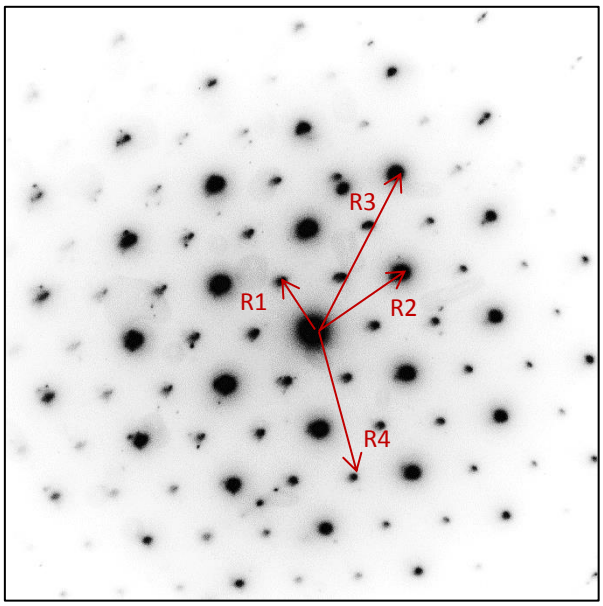

Figure 4-28: Inverted diffraction pattern from 2 – low T. The red arrows indicate the distances measured to calculate d-spacings. The camera length was 66 cm.

Figure 4-28 illustrates the different distances measured on the diffraction pattern, while Table 4-3 gives the distances measured and the calculated d-values. The d-values corresponding to the weaker spots, R_1 and R_4 in the figure, did not match any literature data for BCC-iron, Fe_4N or Fe_3N. The stronger spots, R_2 and R_3, had d-values that corresponded to 110 and 211 of Fe_4N.

Table 4-3: Calculated d-values from the diffraction pattern in Figure 4-28.

	Measured distance [cm]	**Calculated d-value [nm]**	**Literature d-value [nm]**	**hkl**	**Calibrated L [cm]**
R1	0.341	0,485806	?		
R2	0.6	0.2761	0.26885	110	64,2
R3	1.025	0,16162	0,1550	211	63,3
R4	0.925	0,179092	?		

The diffraction pattern was indexed according to a primitive cubic structure along the [111]-zone axis of a Fe_4N-grain, with the lower intensity diffraction spots appearing as extra spots. Figure 4-29 is a partly indexed diffraction pattern with the extra spots marked with arrows.

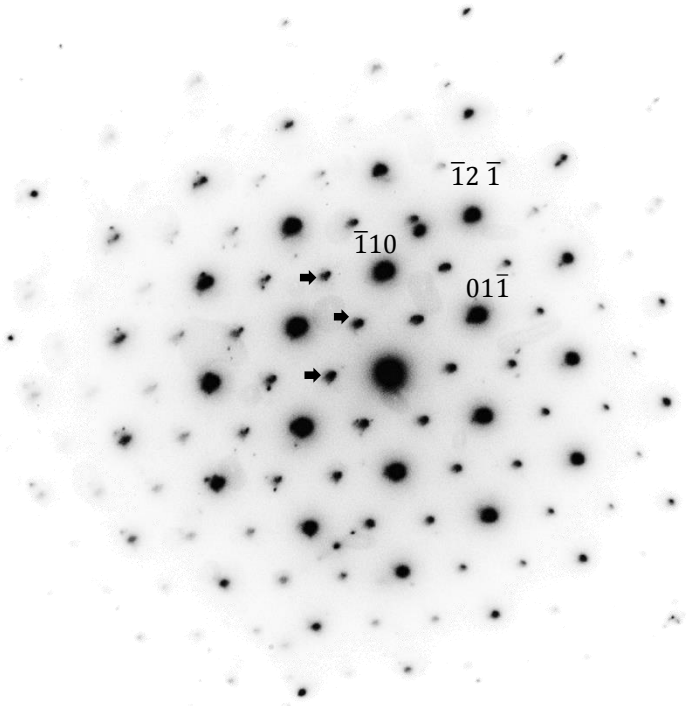

Figure 4-29: Inverted diffraction pattern from the [111] zone-axis of a Fe4N grain at the PPN surface of 2 – low T. The pattern is indexed according to a primitive cubic unit cell along the [111]-zone axis. Some of the extra spots marked with arrows.

5 Discussion

5.1 Compound layer and diffusion zone

The four different PPN conditions, described in 3.1, were supposed to result in one sample with a thin compound layer with an oxide layer on top (1–rough), two samples with a thin compound layer (1-smooth and 2-low T) and one sample with no compound layer (3-no CL). The results are presented in Table 5-1.

Table 5-1: Overview of the compound layer and diffusion zone thickness and core and surface hardness values for all the samples investgated in this project.

Sample	Surface hardness	Core hardness	CL thickness (µm)	DZ thickess (µm)
1 - rough	781 HV1	396 HV0.2	1.2 - 2.3	138
1 - smooth	733 HV0.2	345 HV0.2	~ 2.3	131
2 - low T	788 HV0.2	350 HV0.2	1 - 1.9	62
3 - no CL	707 HV0.2	329 HV0.2	~ 0.2	106

5.1.1 Rough surface sample, PPN condition 1

The oxide layer on 1-rough was not visible in the VLM, as can be seen in Figure 4-2. Nital should etch oxide layers dark, but since the mounting material also appears dark and the oxide layer would be very thin it would be difficult to discriminate between the two. To get a better image of an eventual oxide layer the sample could have been wrapped in copper foil to improve the contrast, but this was not done.

SEM analysis showed charging of the surface and this caused the image to drift. EDS analysis would not be accurate enough to determine the presence of an oxide layer under these conditions, since it would collect oxygen signals from the mounting material. Since the mounting material consists of oxides, EDS analysis taken when the sample drifts would not be accurate enough to determine the presence of an oxide layer. An example of this drift can be seen in Figure 4-4

A SEM with good resolution could be able to image the oxide layer and discriminate it from the nitride compound layer of the steel, since density of the two compounds is different. Iron oxide has a density of between 5.17 and 5.74 g/cm^3 while Fe_3N and Fe_4N has a density of 7.16 and 7.24 g/cm^3 respectively [54-56]. Iron oxide should appear darker than the iron nitrides in a BSE-SEM-image because of the lower density. No such observations were done in this project.

The compound layer and the steel itself has a very weak contrast difference in the BSE-images from SEM. Iron is a heavier element than nitrogen and should scatter more electrons. When nitrogen enters the iron lattice it expands the lattice and the resulting density of the compounds is slightly lower than pure iron (7.87 g/cm^3 [57]), which causes the nitride compound layer to appear slightly darker.

Figure 4-1 and Figure 4-2 shows an uneven compound layer. This could be caused by contamination of small sand particles from the sand blowing of the sample surface before PPN. The growth of the nitride layer is a nucleation process and growth happens at nucleation centres. Imperfections at the surface and contaminant grains will act as nucleation centres and growth will happen more rapidly in these areas.

It is also possible that the oxidizing treatment at the end of the PPN could cause the layer to be uneven. The oxide layer could grow at the expense of the nitride layer, but since no evidence of an oxide layer could be found this is pure speculation.

5.1.2 Smooth surface sample, PPN condition 1

The smooth surface sample shows a much more uniform compound layer, as can be seen in Figure 4-5. This indicates that the polished surface had fewer impurities and this lead to an even growth. This compound layer is about 0.5 µm thicker than the compound layer of 1-rough. A possible explanation for this is the absence of the oxidizing step and therefore no oxide layer growing at the expense of the nitride layer. The diffusion zone depths of the two samples are similar (Figure 4-16 and Figure 4-17) and this supports the assumption of the oxide layer growing at the expense of the nitride layer at the end of the nitriding process of the rough surface sample.

5.1.3 PPN condition 2, low temperature treatment

The low temperature treatment resulted in a thin, uneven compound layer, as can be seen in Figure 4-9. This could indicate that the surface had several impurities or cracks, but could also be a result of the low temperature treatment. Lower temperature slows the growth rate of the nitride compound layer and it is possible that this resulted in an increased growth rate at favourable nucleation centres and a decreased growth in unfavourable areas.

The diffusion zone of this sample is the shortest one of the set and the surface hardness is the highest, and this may provide less protection against HE. The parameters of the PPN-process should be adjusted to increase the diffusion zones depth for maximum protection.

5.1.4 PPN condition 3, no compound layer

PPN condition 3 gave a very thin compound layer, as seen in Figure 4-12. This shows that the PPN treatment did not result in a sample without a compound layer. To achieve this goal the PPN parameters needs to be adjusted. The plasma could be diluted more or the PPN time decreased. The surface is the softest of the four samples, which could indicate that the compound layer was formed at the end of the process and that a decrease in nitriding time could give the desirable result.

The compound layer itself is even and uniform, indicating a clean surface before PPN. This could also be an observation error due to the compound layer size, because the VLM could not magnify the compound layer to an order where the uniformity could be thoroughly examined.

The diffusion zone is larger than in the 2- Low T sample, which can be a result of the diluted plasma. The diluted plasma can make it difficult for the compound layer to grow and more nitrogen diffuses into the iron as a result.

5.2 Compound layer structure

5.2.1 XRD results

The results form XRD shows the presence of α-iron, Fe_3N and Fe_4N in all three samples, although the intensities suggest different distribution. As calculated in Table 3-3, the Mo_α x-

rays penetrate from ~ 1-3 µm into the sample, so it is expected that the upper parts of the diffusion zone are contributing to the results. This explains the presence of iron peaks in all the diffractograms.

The XRD results from the three samples are presented in Figure 5-1 with the main areas of difference highlighted. The differences are related to the intensities of the different iron nitride peaks.

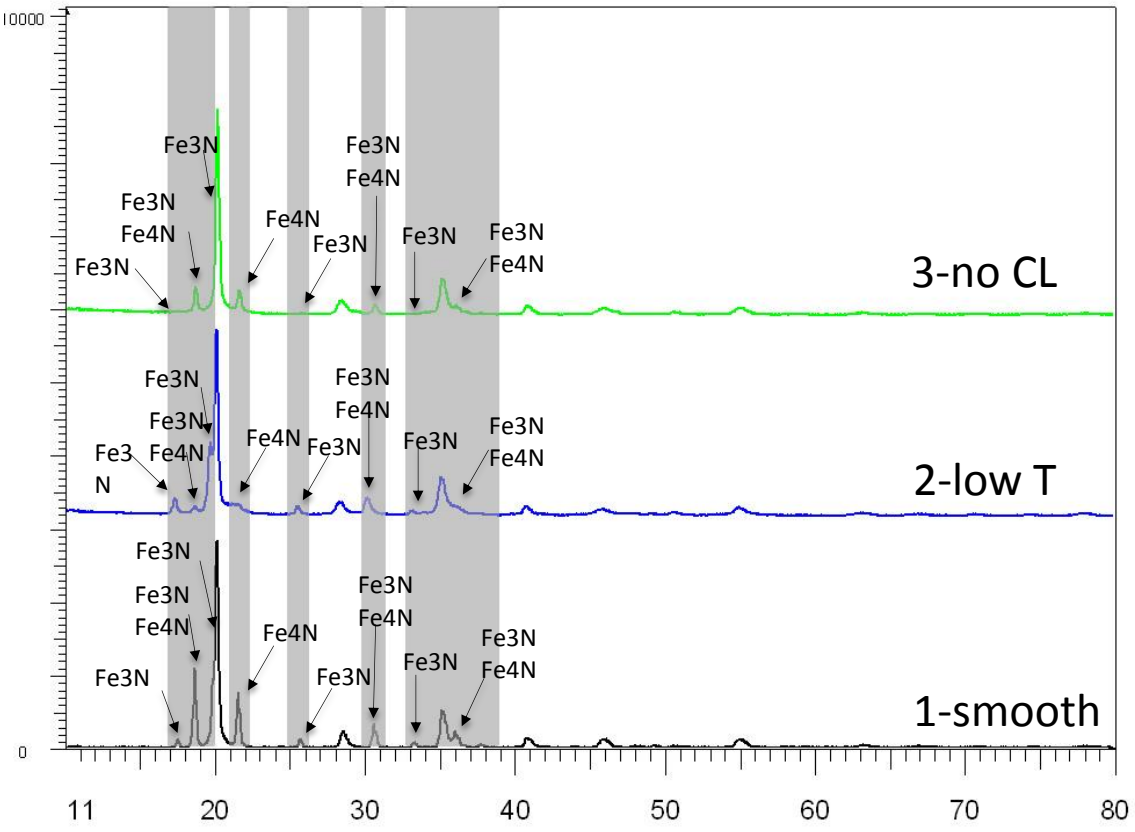

Figure 5-1: XRD data from the three smooth surface samples obtained with Mo_{α}-radiation. The grey areas indicate peaks that differ between the three samples. The iron nitride peaks of interest are marked.

The sample with the thicker compound layer, 1-smooth, have higher intensity on all the nitride peaks, which is as expected, since the sample contains more iron nitride, as can be seen in Figure 4-22. This can also be an effect of the x-rays not penetrating deep enough into the sample to detect a lot of iron.

The Reitveld refinement gives different lattice constants for the iron in the samples. The largest cell parameter belongs to 1-smooth, and is shown to be 2.868 Å. This is the sample with both the largest compound layer and the longest diffusion zone.

The larger lattice constant could be an indication that nitrogen stretches the unit cell, since the sample containing the largest amount of nitrogen shows the largest cell-parameter. The different lattice paramteres could also be an effect of the martensitic structure of the steel. Martensite is a strained form of α-iron and could explain the differences in the cell parameters. The difference could also stem from deformation resulting from the cutting of the samples.

The sample with the smallest compound layer, 3 – no CL, exhibits the smallest lattice constant, 2.854 Å. The diluted plasma and lower temperature of this PPN treatment relates well to an assumption of less nitrogen in the sample, if this is the reason for the smaller lattice. The XRD-result also has the lowest intensities for the nitride peaks.

3 – no CL also has a lower surface hardness than the two other samples, and this could indicate a lower nitrogen content, as discussed in 5.1.4. This in turn could cause less stretching of the unit cell due to nitrogen and therefore lead to a lower cell parameter.

5.2.2 Extra diffraction spots in 2 - Low T

The diffraction pattern from the compound layer of 2 – Low T had several diffraction spots that could not be assigned to the any of the d-values in the reported structures for α-iron, Fe_3N or Fe_4N. A simulated diffraction pattern for the [111] - zone axis of Fe_4N is presented to the left in Figure 5-2, with an image of the obtained diffraction pattern with the extra spots circled to right.

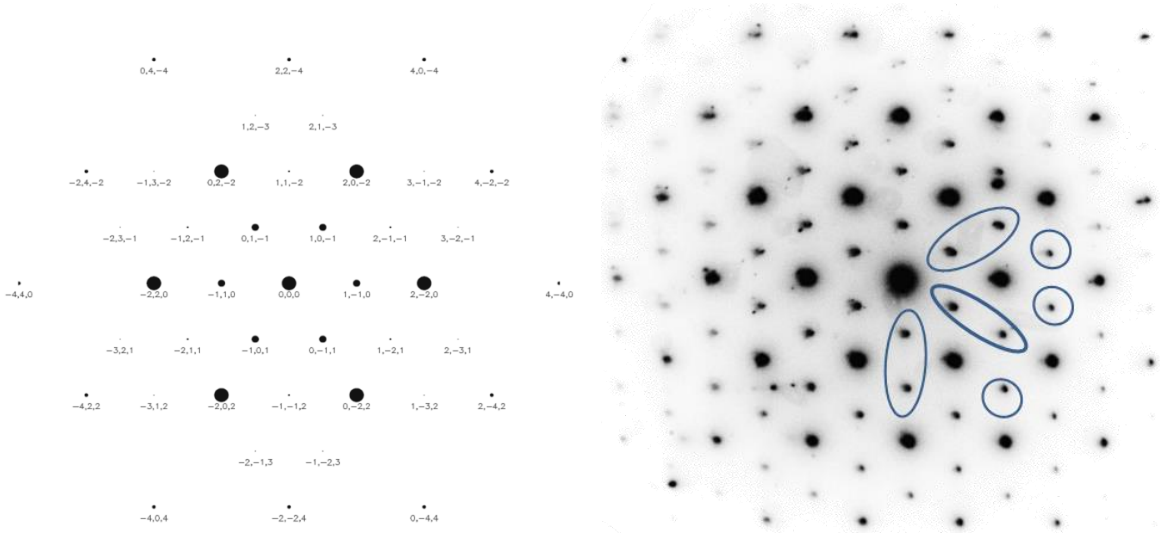

Figure 5-2: Simulated diffraction pattern for Fe_4N. Simulation done with WebEmaps [58]. The diffraction pattern obtained from 2-low T has extra spots, some of which are circled.

The diffraction patterns are similar; the only difference is the measured distances of the circled spots do not correspond to values given in literature. It can therefore be assumed that that these spots represent an external ordering of elements that can be represented with a larger unit cell.

If the obtained diffraction pattern is indexed according to a primitive cubic unit cell, with the extra spots being labelled 110, the lattice parameter of the larger unit cell can be calculated with equation (2-7). With this indexing, as shown in Figure 5-3, the lattice constant of the larger unit cell is found to be 6.58 Å, compared to the literature lattice constant of 3.79 Å. The literature d-value is used in this calculation since the camera length of the microscope is not calibrated.

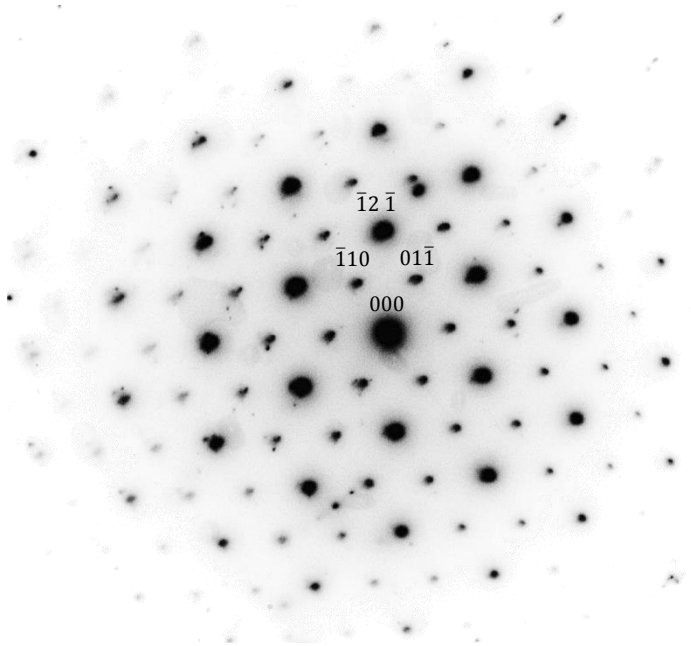

Figure 5-3: Diffraction pattern indexed according to a primitive cubic cell along the [111]- zone axis.

The larger unit cell can be caused by ordering of impurities like oxygen, or be a long range ordering of the nitrogen atoms. Superstructural ordering of N atoms has been reported for both Fe3N and Fe_4N [59-61] so it is possible that this could be the reason for the enlarged unit cell observed in this project.

5.3 Suggestions for further work

The XRD data obtained in this project contains a lot of information that could be extracted with further refinement of the results. XRD should also be obtained from an untreated sample to examine the original lattice constant of the iron. This could lead to a better evaluation of the lattice constant changes and give a better foundation for evaluating the micro strain shown in the Rietveld-refinement.

TEM-investigation of all the PPN conditions is needed to get a better understanding of the compound layers formed after these treatments. In this project it was found that the samples were ion milled to electron transparency at three different places on the sample at the same time. This makes it possible to prepare a sample that gives a good look at the compound layer and the diffusion zone at different depths.

One way to examine the diffusion zone and compound layer at different depths is to prepare several different samples of the same PPN condition and ion mill them at different times to create different sized hole. Another way is to prepare one sample for each PPN condition, and ion mill it to a small hole can be observed; investigate this sample in the TEM; and ion mill the sample again before re-examining it. The advantage with the last method is that information from the same areas of the sample surface can be investigated at different depths and the disadvantage is that the areas examined are destroyed with further ion milling to reveal areas deeper into the sample.

The possible observation of superstructure in Fe_4N in 2- Low T needs to be investigated further to determine what causes the extra diffraction spots. Diffraction from other zone-axes and more simulation can lead to a suggested expanded unit cell and TEM investigation of other grains and areas of the sample can give an indication of how common this external ordering is. It is also interesting to investigate the other PPN-conditions to see if the same phenomenon can be seen there.

6 Conclusions

This project has shown that the four different PPN treatments resulted in four compound layers and diffusion zones with different thickness, as expected.

The PPN treatment that was supposed to result in a sample with no compound layer exhibited a very thin surface layer of about 0.2 µm. To achieve the goal of a PPN process that results in no compound layer, the parameters have to be adjusted with either a dilution of the plasma, or a reduction of the nitriding time.

XRD analysis revealed that all the samples consisted of the three phases; α-iron, Fe_3N and Fe_4N, but the intensities indicated different ratios. Closer examination of the XRD-results could give more information about the cell parameters of the compounds and their relative ratios.

TEM of 2- Low T revealed grains in the size order of a few 100 nm at the compound layer surface.

Electron diffraction showed extra diffraction spots corresponding to a primitive cubic lattice with a cell parameter of 6.58 Å. Further investigation is needed to decide what causes the external ordering and to create a model of the expanded unit cell.

References

1. Thomas C. Shirley, J.W.T., Jr., Fabio Moretzsohn, Jorge Brenner, *Biodiversity of the Gulf of Mexico: Applications to the Deep Horizon oil spill*. 2010, Harte Research Institute for Gulf of Mexico Studies.
2. Wikipedia. *Economic effects of the Deepwater Horizon oil spill*. 2013 [cited 2013 24.08.2013]; Available from: http://en.wikipedia.org/wiki/Economic_and_political_consequences_of_the_Deepwater_Horizon_disaster.
3. Michelangelo Fabbrizzi, P.D.S., Robert Merlo. *A Method for the Verification of Subsea Equipment Subject to Hydrogen Induced Stress Cracking*. in *ASME 2010 29th International Conference on Ocean, Offshore and Arctic Engineering*. 2010. Shanghai, China.
4. Gunnæs, A.E., et al., *Grant proposal - Fundamental studies of the effect of pulsed plasma modification of steel surfaces (FEPPS)*. 2009.
5. Oriani, R.A., *Whitney award lecture 1987 - Hydrogen - The versatile embrittler.* Corrosion, 1987. **43**(7): p. 390-397.
6. Johnson, W.H., *On Some Remarkable Changes Produced in Iron and Steel by the Action of Hydrogen and Acids.* Proceedings of the Royal Society of London, 1874-1875. **23**.
7. Johnson, W.H., *On Some Remarkable Changes Produced in Iron and Steel by the Action of Hydrogen and Acids.* Nature, 1875. **11**.
8. Oriani, R.A. and Oriani, *Hydrogen embrittlement of steels.* Annual review of materials science, 1978. **8**(1): p. 327-357.
9. Norby, T., *Materialer og energi*. 2006, [Oslo]: Det matematisk-naturvitenskapelige fakultet, Universitetet i Oslo.
10. Key to metals. *Engineering Stress-Strain Curve: Part One*. [cited 2012 02.11]; Available from: http://www.keytometals.com/page.aspx?ID=CheckArticle&site=kts&NM=43.
11. HSC, N. *Tensile testing*. [cited 2012 01.11]; Available from: http://hsc.csu.edu.au/engineering_studies/application/lift/3210/index.html.
12. Almar-Næss, A., *Metalliske materialer*. 1993, [Trondheim]: Tapir. XVI, 464 s. : ill.
13. Kopeliovich, D. *Plastic deformation*. 2012 2012.05.31 [cited 2012 13.11]; Available from: http://www.substech.com/dokuwiki/doku.php?id=plastic_deformation.
14. Robertson, I.M. and H.K. Birnbaum. *Dislocation mobility and hydrogen - a brief review*. in *11th International Conference on Fracture*. 2005. Turin (Italy).
15. Robertson, I.M., *The effect of hydrogen on dislocation dynamics.* Engineering Fracture Mechanics, 2001. **68**(6): p. 671-692.
16. Dadfarnia, M., et al., *Recent Advances in the Study of Structural Materials Compatibility with Hydrogen.* Advanced Materials, 2010. **22**(10): p. 1128-1135.
17. Barnoush, A., *Hydrogen embrittlement*. 2011.
18. Ferreira, P.J., I.M. Robertson, and H.K. Birnbaum, *Hydrogen effects on the interaction between dislocations.* Acta Materialia, 1998. **46**(5): p. 1749-1757.
19. Beachem, C.D., *New model for hydrogen-assisted cracking (hydrogen embrittlement).* Metallurgical Transactions, 1972. **3**(2): p. 437-.
20. Lynch, S.P., *Mechanisms of hydrogen-assisted cracking.* Metals Forum, 1979. **2**(3): p. 189-200.

21. Oriani, R.A., *Hydrogen Embrittlement of Steels*. Hydrogen Embrittlement and Stress Corrosion Cracking, ed. R. Gibala, R.F. Hehenmann, and R.F. Hehemann. 1984: ASM International.
22. Vehoff, H. and W. Rothe, *Gaseous hydrogen embrittlement in FeSi-single and Ni-single crystals.* Acta Metallurgica, 1983. **31**(11): p. 1781-1793.
23. Kofstad, P. and T. Norby, *Defects and transport in crystaline solids*. 2012, University of Oslo: Oslo.
24. Tilley, R., *Understanding Solids - The Science of Materials*. 2004: John Wiley & Sons
25. Zakroczymski, T., N. Lukomski, and J. Flis, *Entry and Transport of Hydrogen in Ion Nitrided Iron.* Journal of The Electrochemical Society, 1993. **140**(12): p. 3578-3583.
26. Zakroczymski, T., N. Lukomski, and J. Flis, *The effect of plasma nitriding-base treatments on the absorption of hydrogen by iron.* Corrosion Science, 1995. **37**(5): p. 811-822.
27. Bruzzoni, P., et al., *Hydrogen permeation modification of 4140 steel by ion nitriding with pulsed plasmas.* Surface and Coatings Technology, 1998. **110**(1–2): p. 13-18.
28. Cwiek, J., *Plasma nitriding as a prevention method against hydrogen degradation of steel.* Journal of Achievements in Materials and manufacturing Engineering, 2009. **36**(1).
29. Wolarek, Z. and T. Zakroczymski, *Hydrogen absorption in plasma-nitrided iron.* Acta Materialia, 2006. **54**(6): p. 1525-1532.
30. Weidmann, E., A. Guesnier, and S. A/S, *Metallographic preparation of nitrided and nitrocarburised components - Application notes*, Struers, Editor. 2006, Rosendahls bogtrykkeri: Denmark.
31. Ochoa, E.A., et al., *Microstructure and properties of the compound layer obtained by pulsed plasma nitriding in steel gears.* Surface and Coatings Technology, 2009. **203**(10–11): p. 1457-1461.
32. Díaz-Guillén, J.C., et al., *Surface Properties of Fe4N Compounds Layer on AISI 4340 Steel Modified by Pulsed Plasma Nitriding.* Journal of Materials Science & Technology, 2013. **29**(3): p. 287-290.
33. Torkar, M. and V. Leskovšek, *Pulsed-plasma nitriding of Fe-12.5 Al alloy.* Intermetallics, 1995. **3**(5): p. 427-430.
34. Hoel , R.H., *Tynnfilm og pulsplasma*. 2013.
35. Barnoush, A., et al., *Hydrogen Effect on Nanomechanical Properties of the Nitrided Steel.* Metallurgical and Materials Transactions a-Physical Metallurgy and Materials Science, 2013. **44A**(2): p. 766-775.
36. Barnoush, A. and H. Vehoff, *Electrochemical nanoindentation: A new approach to probe hydrogen/deformation interaction.* Scripta Materialia, 2006. **55**(2): p. 195-198.
37. Asgari, M., et al., *Nanomechanical evaluation of the protectiveness of nitrided layers against hydrogen embrittlement.* Corrosion Science, 2012. **62**(0): p. 51-60.
38. Matar, S., et al., *The calculated electronic and magnetic structures of Fe4N and Mn4N.* J. Phys. France, 1988. **49**: p. 1761-1768.
39. Jacobs, H., D. Rechenbach, and U. Zachwieja, *Structure determination of γ'-Fe4N and ϵ-Fe3N.* Journal of Alloys and Compounds, 1995. **227**(1): p. 10-17.
40. Barron, A.R. and C. Smith, *Crystal structure - Bravais lattices*. 2010.
41. Williams, D.B. and C.B. Carter, *Transmission Electron Microscopy*. 2nd ed. Vol. 1. 2009: Springer.
42. Stokkan, T.S., *Structural investigation of a Ni-Nb-O phase by electron diffraction*. 2011, University of Oslo: Oslo.
43. Karlsen, O.B., *Røntgendiffraksjon del 1 - forelesningsnotater MENA3100*. 2013.

44. Fjeld, H. and A.W.B. Skilbred, *Scanning electron microscope - Lecture notes for MENA3100*. 2013.
45. Versluijs, M. *Inorganic chemistry UU - Research Programme design*. [cited 2013 24.04]; Available from: http://www.anorg.chem.uu.nl/people/staff/MarjanVersluijsHelder/home.htm.
46. Bagshaw, H. *Scanning electron microscopy*. 2012 [cited 2013 27.09]; Available from: http://www.tcd.ie/CMA/misc/Scanning_electron_microscope.pdf.
47. Gringer, *Scheme TEM*. 2009, Wikipedia.
48. Brandon, D. and W.D. Kaplan, *Microstructural Characterization of Materials*. Second ed. 2008: John Wiley & Sons, Ltd.
49. Klug, H.P. and L.E. Alexander, *X-ray diffraction procedures - For polycrystalline and amorphous materials*. Second edition ed. 1974, USA: John Wiley Sons.
50. *International tables for crystallography*, ed. A.J.C. Wilson. Vol. Volume C - mathematical, physical and chemical tables. 1992, Dordrecht/Boston/London: Kluwer academic publishers.
51. Wikipedia. *Hardness*. 2012 [cited 2013 16.03]; Available from: http://en.wikipedia.org/wiki/Hardness.
52. Wikipedia. *Indentation hardness*. 2013 [cited 2013 16.03]; Available from: http://en.wikipedia.org/wiki/Indentation_hardness.
53. Normung, D.I.F., *DIN 50190-4 Ermittlung der Nht*. 1996.
54. Wikipedia. *Iron(III) oxide*. 2013 [cited 2013 29.09]; Available from: http://en.wikipedia.org/wiki/Iron%28III%29_oxide.
55. Wikipedia. *Iron(II) oxide*. 2013 [cited 2013 29.09]; Available from: http://en.wikipedia.org/wiki/Iron%28II%29_oxide.
56. Wikipedia. *Iron(II,III) oxide*. 2013 [cited 2013 29.09]; Available from: http://en.wikipedia.org/wiki/Iron%28II,III%29_oxide.
57. Wikipedia. *Iron*. 2013 [cited 2013 25.09]; Available from: http://en.wikipedia.org/wiki/Iron.
58. Zuo, J.M. and J.C. Mabon. *Web-based Electron Microscopy Application Software: Web-EMAPS*. 2004; Available from: http://emaps.mrl.uiuc.edu/.
59. Liu, Z.Q., et al., *Transmission electron microscopy study on the superstructure and the precipitation of γ'-Fe4N in initially homogeneous ε-iron nitride powders.* Journal of Materials Science, 2006. **41**(9): p. 2673-2677.
60. Nagakura, S., *Electronic Structure of Iron Nitrides Studied by Electron Diffraction. I. γ'-Fe4N.* Journal of the Physical Society of Japan, 1968. **25**(2): p. 488.
61. Liu, Z.Q., *Study of Microstructure and Nitride in Ion-nitrided Pure Iron with High Resolution Electron Microscope*. 2000, Dalian Maritime University.